Probabilistic Tsunami Hazard Assessment for a Site in Eastern Canada

Vikram Kulkarni,[1] Maria E. M. Arcos,[1] Trajce Alcinov,[2] Alexis Lavine,[1] Robert Youngs,[1]
Patrick Roussel,[2] and Derek Mullin[3]

Abstract—Unlike probabilistic seismic hazard analysis (PSHA), there is not a well-established methodology for probabilistic tsunami hazard analysis (PTHA). The PTHA methodology presented is similar to the widely used PSHA methodology for ground motion, and incorporates both aleatory and epistemic uncertainty in calculating the probability of exceeding runup and drawdown values produced by tsunamigenic sources. Evaluating tsunami hazard is more difficult in locations such as the eastern coastline of Canada because of low tsunami recurrence rates and few historical examples. In this study, we evaluated the hazard from local and far-field earthquake and landslide tsunamigenic sources at a site on the Bay of Fundy in New Brunswick, Canada. These sources included local faults, the Puerto Rico subduction zone, fault sources in the Azores-Gibraltar plate boundary region, and landslides on the Canadian continental slope and in the Canary Islands. Using a new PTHA methodology that is closely linked to well-established PSHA methodology combined with tide stage probability, we calculated that the return period for a wave runup exceeding the tidal range of +4 m level above mean sea level (highest astronomical tide) is approximately 14,500 years.

Key words: Tsunami, Atlantic, Canada, probabilistic, hazard, modelling, PTHA.

1. Introduction

The Atlantic coastline of North America in general, and the Canadian coastline in particular, historically has had few tsunami events and has, therefore, received less attention in tsunami hazard studies than more tsunami prone regions on the Pacific coast. In addition, because there have been few events, many tsunami sources affecting the Atlantic coastline are poorly constrained. However, there are many large population centers and infrastructure along this coastline that could be severely impacted in a tsunami event.

The preliminary tsunami hazard assessment of the Canadian coastline by Leonard et al. (2012) demonstrated that the overall tsunami hazard for the outer Atlantic coastline of Canada is an order of magnitude lower than that of the outer Pacific coastline of Canada, but an order of magnitude higher than that of the Arctic coastline. Building on Leonard et al. (2012) the aim of this study is to characterize the site-specific, probabilistic tsunami hazard in the vicinity of the Point Lepreau peninsula in New Brunswick (Figs. 1, 2), considering the contributions of all potentially significant sources throughout the Atlantic Ocean in a probabilistic tsunami hazard analysis (PTHA). The Point Lepreau peninsula was selected as the location of interest, as it is adjacent to the Point Lepreau Generating Station (PLGS), the only nuclear power plant on the Atlantic Coast of Canada.

PTHA uses a well-established methodology developed for probabilistic seismic hazard analysis (PSHA). Modern PSHA address both the inherent randomness of the physical process (termed aleatory uncertainty or aleatory variability) and the scientific uncertainty in defining models and model parameters to represent the physical process (termed epistemic uncertainty). In most PSHA studies the epistemic uncertainty is incorporated using the logic tree methodology (e.g., Kulkarni et al. 1984) in which alternative models and model parameters are assigned relative weights based on scientific merit and/or statistical analysis. These relative weights are then applied to the hazard computed from each set of

---

[1]   Amec Foster Wheeler, 180 Grand Avenue, Suite 1100, Oakland, CA 94612, USA.
[2]   Amec Foster Wheeler, 50 Troop Avenue, Dartmouth, NS B3B 1Z1, Canada. E-mail: trajce.alcinov@amecfw.com
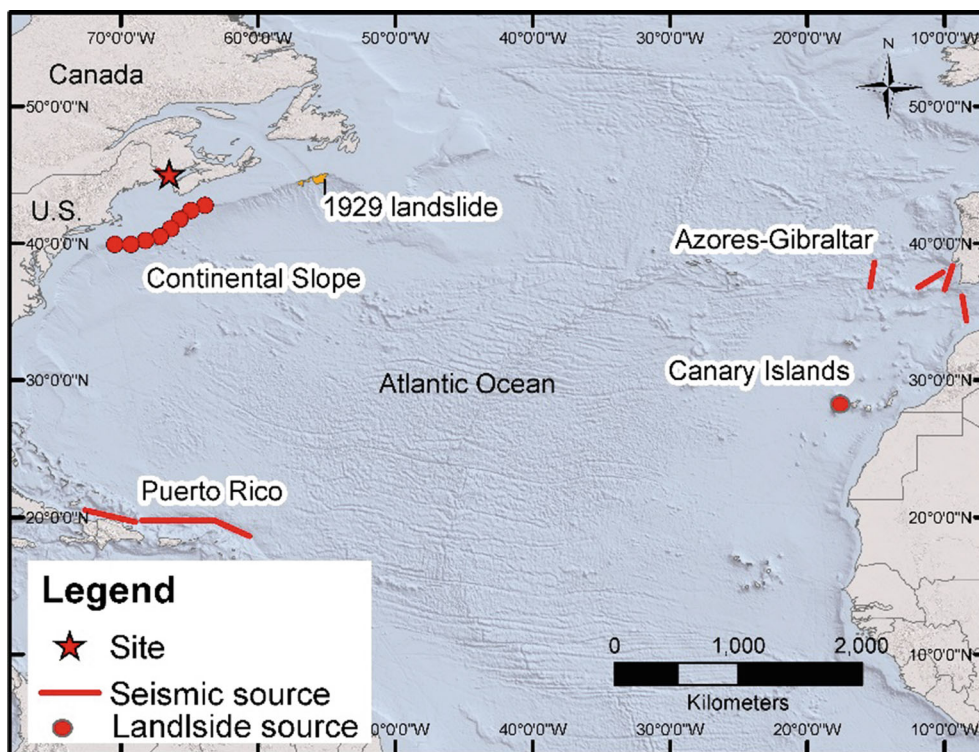[3]   NB Power, P.O. 600, Lepreau, NB E5J 2S6, Canada.

Figure 1
Locations of far-field landslide and fault sources simulated in this study. Topography and Bathymetry from ETOPO1 (Amante and Eakins 2009). 1929 tsunami source based on zone of 100% failure from Mosher and Piper (2007b)

alternative input parameters to produce a composite weighted hazard result. Most PTHA studies include elements of PSHA methodology but there is not a single established PTHA methodology.

One key aspect of this study is the use of a PTHA methodology that is as analogous as possible to the more widely used PSHA. The use of this methodology includes development of scaling relationships, which allow us to use low hazard scenarios. Our model explicitly includes epistemic uncertainty through the use of logic trees and produces results similar to those typically developed for PSHA.

Several studies have developed PTHA methodologies (e.g., Maretzki et al. 2007; González et al. 2009; Thio et al. 2010), but PTHA includes challenges not encountered in PSHA. Factors that add to the difficulty of PTHA include: (1) Modeling tsunamis is computationally intensive. Most previous studies have either limited the number of potential sources, not modeled tsunami inundation or not included landslide sources; (2) Tsunami sources and

landslide-generated tsunamis in particular are not well constrained due to few historical events and landslides having more model input parameters than earthquakes; (3) There are potentially many more sources to characterize for PTHA than PSHA because all tsunami sources in the ocean basin should be considered rather than all sources within the distance of concern decided for a PSHA.

2. PTHA Methodology

The mathematical formulation used for the PTHA follows the methodology first proposed by Cornell (1968, 1971) for PSHA. Assuming that the occurrence of damaging events can be represented as a Poisson process, the probability that a hazard parameter (either runup or drawdown), Z, will exceed a specified value, z, in time period t is given by:

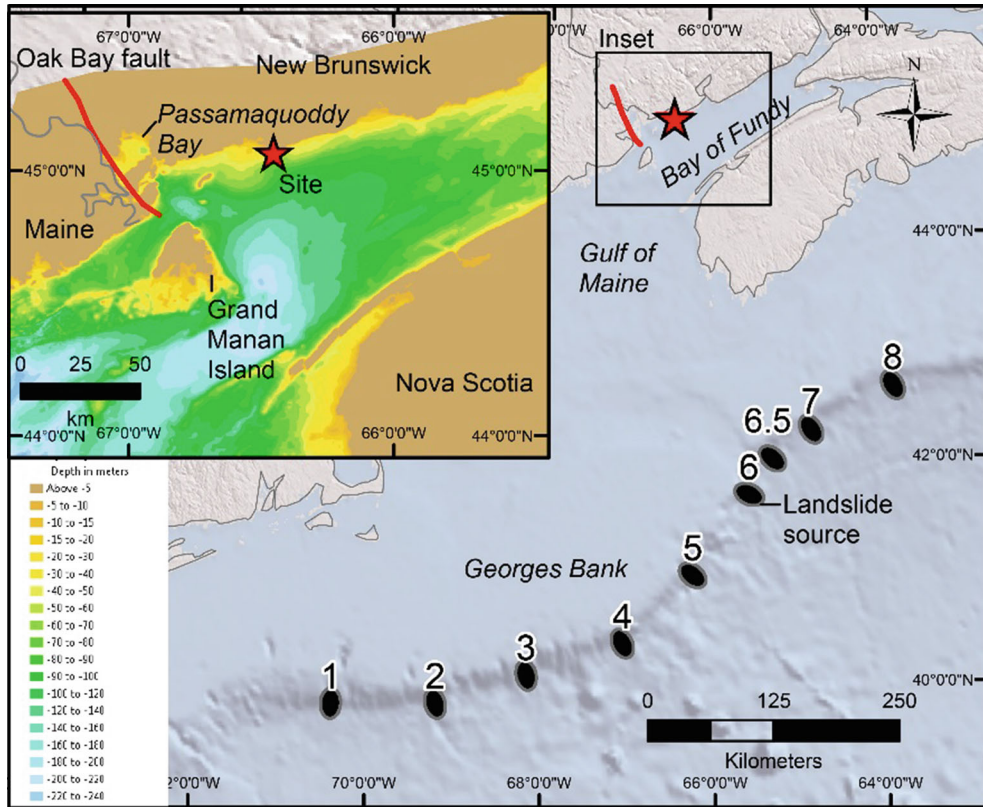$$P(Z > z|t) = 1.0 - e^{-v(z) \cdot t} \leq v(z) \cdot t, \qquad (1)$$

Figure 2
Location of the Oak Bay fault, continental slope deterministic sources and site. Oak Bay fault trace is based on Gates (1989). Topography and bathymetry are ETOPO1 (Amante and Eakins 2009) and inset bathymetry of the Gulf of Maine (Roworth and Signell 1999)

where $v(z)$ is the average frequency during time period t at which the hazard parameter Z exceeds value z at the site resulting from all events on all sources in the region.

The hazard computation focuses on the computation of the annual frequency of exceedance $v(z)$. In concept, we combine the annual rate of events generating a tsunami with the distribution of amplitudes that are expected to exceed value z at the site for a given tsunami. The approach is a function of the frequency of event occurrence, the randomness of size of future events, and the randomness in the level of wave heights they may produce at the site.

For earthquake sources, it is computed by the expression:

$$v_{EQ}(z) = \sum_n \alpha_n(m^0) \int_{m^0}^{m^u} f(m) \cdot P(Z > z|m)\mathrm{d}m \quad (2)$$

where $\alpha_n(m^0)$ is the annual frequency of earthquakes on source n above a minimum magnitude of engineering significance, m^0; $f(m)$ is the probability density of earthquake size between m^0 and a maximum earthquake the source can produce, m^u; and $P(Z > z|m)$ is the probability that, given an earthquake of magnitude m at the source, the peak runup or drawdown will exceed level z.

Equation 2 is used in its discrete form:

$$v_{EQ}(z) = \sum_n \left\{ \sum_{m^0}^{m^u} \lambda_n(m_i) \cdot P(Z > z|m_i) \right\}. \quad (3)$$

The term $\alpha_n(m^0) \cdot f(m)$ in Eq. 2 becomes $\lambda_n(m_i)$ in Eq. 3. It is the annual frequency of earthquakes on source n with magnitudes $m_i \pm \Delta m/2$. The magnitude discretization step size Δm is set at 0.1 magnitude units. The magnitude frequencies $\lambda_n(m_i)$ are obtained using the cumulative earthquake recurrence

relationships to compute the cumulative earthquake recurrence rates for magnitudes $m_i - \Delta m/2$ and $m_i + \Delta m/2$. The difference in these two values provides the discrete annual rate for earthquakes in the magnitude range $m_i - \Delta m/2$ to $m_i + \Delta m/2$.

The other term of Eq. 3, $P(Z > z|m_i)$, provides the probability that an earthquake of magnitude m_i at the source will produce amplitudes in excess of the specified value of peak wave runup or drawdown, z. It is used to represent the natural variability (aleatory uncertainty) observed in the expected wave amplitudes. This aleatory uncertainty is nearly always modelled by a lognormal distribution (e.g., McGuire 2004). The median of $\ln(z)$ for given values of m_i, termed $\ln(W_{tsu}|m_i)$, is obtained using linear regression relationships and the standard deviation of $\ln(z)$, termed σ_{EQ}, is computed for each source. The standard cumulative normal probability function is then used to compute $P(Z > z|m_i)$ as unity minus the probability that the peak ground motion amplitude is less than $\ln(z)$.

$$P(Z > z|m_i) = 1 - \Phi\left(\frac{\ln(z) - \ln(W_{tsu}|m_i)}{\sigma_{EQ}}\right) \quad (4)$$

The earthquake magnitude parameter, m, is expressed in Eqs. (2) and (3) above as the parameter upon which the probability of peak wave runup exceeding a specified level, z [i.e. $P(Z > z)$] is dependent. Since values of $P(Z > z)$ are conditional to a given earthquake magnitude size (m_i), we term such a parameter as a "conditional parameter" within our formulation.

There are parameters other than earthquake magnitude within the tsunami initiation model that may contribute to aleatory uncertainty. These parameters are also correlated to varying degrees to earthquake magnitude. Earthquake magnitude is used as a conditional parameter because it captures event size and is the parameter cataloged extensively in event records, making it suitable to develop recurrence estimates. Methods for including the aleatory uncertainty of other parameters are discussed in the Sect. 2.4 further below.

For landslide sources, the hazard computation is carried out in a fashion analogous to the earthquake sources. It is computed by the expression:

$$v_{LS}(z) = \sum_n \alpha_n(vol^0) \int_{vol^0}^{vol^u} f(vol) \cdot P(Z > z|vol) dvol \quad (5)$$

Note that the variable vol is the natural logarithm of the landslide volume in km^3. $\alpha_n(vol^0)$ is the annual frequency of landslide events on source n above a $\ln$[minimum volume] of engineering significance, vol^0; $f(vol)$ is the probability density of landslide event size between vol^0 and a $\ln$[maximum landslide size] that the source can produce, vol^u; and $P(Z > z|vol)$ is the probability that, given an event of $\ln$[volume size] vol at the source, the peak wave height will exceed level z.

In the hazard model, Eq. (5) is used in its discrete form:

$$v_{LS}(z) = \sum_n \left\{ \sum_{vol^0}^{vol^u} \lambda_n(vol_i) \cdot P(Z > z|vol_i) \right\}. \quad (6)$$

The term $\alpha_n(vol^0) \cdot f(vol)$ in Eq. 5 becomes $\lambda_n(vol_i)$ in Eq. 6. It is the annual frequency of earthquakes on source n with $\ln$[volume] $vol_i \pm \Delta vol/2$. The exceedance computation is calculated up to a volume of $200~km^3$—above which the recurrence rate values are not significant.

The rate for landslides, $\lambda_n(vol_i)$, does not distinguish between the mechanism causing the landslides, such as those triggered by earthquakes versus those due to other instability inducing phenomena.

The other term of Eq. 6, $P(Z > z|vol_i)$, is computed in a similar fashion to the earthquake sources.

$$P(Z > z|vol_i) = 1 - \Phi\left(\frac{\ln(z) - \ln(W_{tsu}|vol_i)}{\sigma_{LS}}\right) \quad (7)$$

For landslide sources, landslide volume is termed as the conditional parameter. Similar to the earthquake source formulation, there are parameters other than landslide volume within the tsunami initiation model that may contribute to aleatory uncertainty. These parameters are also correlated to varying degrees to landslide volume. Landslide volume is used as a conditional parameter because it captures event size and is the parameter used in event records of several studies, making it suitable to develop recurrence estimates. Methods for including the aleatory uncertainty of other parameters is discussed

in the "Aleatory Uncertainty of tsunami waves" subsection further below.

2.1. Location Uncertainty

Due to the limited number of scenarios that were implemented for hydrodynamic modeling, location uncertainty was included only if significant impact was observed in the deterministic modelling results. We explored the effects of location uncertainty on the resulting hazard parameters of concern. Sources that were deemed to have significant relative impact based on their location were included in the hazard computation as segmented sources, with weights assigned to each segment based on their lengths. In particular, the Puerto Rico trench earthquakes and the Scotian slope landslide sources consider location uncertainty in their hazard contribution.

2.2. Total Tsunami Hazard Without Tidal Effects

The total hazard due to tsunamis from earthquakes and landslides is the sum of annual frequencies of each of the two source types.

$$v_{Tsu}(z) = v_{EQ}(z) + v_{LS}(z). \qquad (8)$$

2.3. Total Tsunami Hazard Including Tidal Variation

The modelling performed to assess tsunami runup and drawdown provides assessments relative to a specific sea level, e.g., mean sea level (MSL) or highest astronomical tide (HAT), and the values of $P(Z > z)$ are computed assuming that that water level is present. However, there is a large daily tidal variation at the site with average annual maximum and minimum tidal levels of nearly ±3.8 m about MSL. As a result, the arrival of a 2 m tsunami wave at high tide is a different event than the arrival of a 2 m tsunami wave when the tidal level is near MSL such that the runup does not produce a water level equal to high tide. Similarly, a drawdown of 2 m from a tsunami represents different contributions to hazard if it occurs at low tide compared to occurring when the tide is at MSL.

Because of the large tidal variation, the total tsunami hazard (including tidal variation) is defined

relative to two reference points. The tsunami runup hazard is defined in terms of runup above +4 m MSL and the tsunami drawdown hazard is defined in terms of drawdown below −4 m MSL. Between these two elevations, annual tidal variation dominates. The formulation for tsunami hazard including tidal variation hazard is:

$$v_{Total}(z) = \sum_{i=1}^{N_T} P(x_i) \cdot v_{Tsu}(Z > z - x_i | x_i), \qquad (9)$$

where z represents water elevation above +4.0 m MSL for wave runup, and water elevation below −4.0 m MSL for drawdown. In Eq. 9, parameter x_i is the tidal level.

Conceptually, Eq. 9 can be considered in this way: the annual frequency of tsunamis producing a wave runup of +6 m MSL (2 m above +4 m MSL) is the sum of the frequency of tsunamis producing greater than 2 m of runup arriving when the tide is near +4 m above MSL, plus the frequency of tsunamis producing greater than 6 m of runup arriving when the tide is near MSL, plus the frequency of tsunamis producing greater than 10 m of runup arriving when the tide is near −4 m MSL. In the actual calculation, the tidal levels are discretized into finer increments of 0.1 m. For each tidal level (x_i) the frequency of tsunamis exceeding a specific runup of ($z - x_i$) is the product of the annual frequency of tsunamis exceeding that runup and the probability that the tide is at tidal level x_i. The probability of various tidal levels is based on using hourly predictions for the tidal variation over 19 years, and computed annual probability of exceedance of tidal levels. The inputs to the probabilistic analysis include results from the deterministic modelling of all considered tsunami events at both high tide and mean sea level, therefore accounting for some of the nonlinearity of tsunami propagation and inundation at different tidal stages.

Equation 9 also includes the conditional aspect that the frequency of various runup (or drawdown) depends on the tidal level x_i. This is incorporated in the analysis by computing the frequency of exceeding various runup values for MSL and HAT water levels and interpolating in logarithmic space between these two levels for other tidal levels.

2.4. Aleatory Uncertainty of Tsunami Waves

Tsunami wave runup and drawdown for all scenarios are computed using numerical models. For such cases, aleatory uncertainty is divided into modelling and parametric components (Abrahamson et al. 1990; PGEC 2010). Aleatory uncertainty must be included in probabilistic hazard models in order to obtain accurate hazard estimates. Exclusion or underestimation of aleatory uncertainty will result in underestimation of the hazard.

2.4.1 Deterministic Modelling Aleatory Uncertainties

Since very few significant tsunami events have occurred in the Atlantic Ocean in recent history, there is a lack of robust knowledge of the geological tsunamigenic mechanisms, as well of the resulting coastal tsunami runup. This limits the prospects for a rigorous evaluation of the performance of Atlantic Ocean tsunami models. Therefore, for the purposes of deriving an estimate of aleatory uncertainty due to the numerical deterministic model deviation from observations, we use as a proxy the results of the numerical modelling work of Ioualalen et al. (2007), who used comparable modelling techniques to the present study, to model the 2004 Indian Ocean tsunami and its impact on Thailand. Ioualalen et al. (2007) performed simulations using the Okada (1985) coseismic deformation model in conjunction with the FUNWAVE model and compared tsunami predictions with tide gauge observations and satellite altimeter data for the 2004 Indian Ocean event in Thailand. They found a 92% correlation between observations and predictions. The root mean squared error (1.05 m) was found to represent 17.24% of the mean observed runup value (6.11 m). This represents a notably low error, comparable to the range of 10–12% errors that Horillo et al. (2014) reported for a variety of Boussinesq and NSW equation models, based on benchmark tests from laboratory experiments. In addition, Ioualalen et al. (2007) studied the effects of frequency dispersion on coastal runup using a NSW model for comparison to the Boussinesq FUNWAVE model, and concluded that dispersive effects were not dominant for the modelled scenario

in coastal Thailand. They found discrepancies between the results of the two models of up to 25% in localized areas, with the most frequent difference being in the range of 10–15%. As such, we consider the performance statistics derived by Ioualalen et al. (2007) to be generally applicable for both the Delft3D model based on the NSW equations, as well as the FUNWAVE-TVD model within the context of the probabilistic tsunami hazard assessment.

Modelling aleatory uncertainty is the difference between the observed values due to an event at a location versus the modelled values of that event at the same location. Modelling aleatory uncertainty was assigned as 17.2 percent of the median observed values—as explained above. This translates to a σ_{ln} value of 0.1587, which is applicable to all cases.

2.4.2 Parametric Aleatory Uncertainties

Parametric aleatory uncertainty is the uncertainty due to the natural randomness of the parameters within the source model. Parameters upon which the probabilistic formulation is not explicitly shown to be dependent (i.e., parameters other than earthquake magnitude for earthquake sources, and landslide volume for landslide sources) are considered under this uncertainty. To be included, these parameters also need to belong to the aleatory uncertainty category. For earthquake sources, we used uncertainty of the slip distribution parameter as the parametric aleatory uncertainty for each source. We assumed that this parameter was uncorrelated to earthquake magnitude (although some correlation exists among them), and thus applied the computed uncertainty without reduction. For landslide sources, we used the landslide slope parameter uncertainty as the parametric aleatory uncertainty. We also assumed that landslide slope was uncorrelated with landslide volume (although some correlation exists among them), and thus applied the computed uncertainty without reduction. Other parameters also exist for both source types that may contribute to parameter uncertainty to some extent, since they are correlated to the conditional parameter in the formulation to some extent. The included parameters had the highest impact at the tsunami initiation point, and choosing them alone but applying their uncertainty without

reduction was considered a reasonable approach. Due to few modeled scenarios developed as part of study, computing uncertainties and correlations for each parameter was not possible. Refer to the Sect. 4.4 for additional discussion regarding parametric aleatory uncertainty.

2.4.3 Regression Aleatory Uncertainties

Linear regressions are used to obtain scaling relationships between the hazard parameter of concern and conditional parameter(s) in the probability of exceedance computation. Regression uncertainty is computed about the regression model and included as a component of the aleatory uncertainty. The regression uncertainty used is the lognormal standard deviation of the prediction error for the predictor of any individual value of the ordinate. This uncertainty considers the random error of the data about the model and the distribution of the mean value of the regression model. This uncertainty increases as the independent variable where prediction is sought moves farther from the sample mean of the observed data of the independent variable.

Total aleatory uncertainty is the square root of the sum of squares of the above three component aleatory uncertainties.

$$\sigma_{\text{Total}} = \sqrt{\sigma_{\text{mod}}^2 + \sigma_{\text{par}}^2 + \sigma_{\text{regr}}^2} \qquad (10)$$

Since the aleatory uncertainty was computed based on limited data, the total aleatory uncertainty at several discretized magnitudes produced values that were judged to be above reasonable limits. The PTHA study for the Diablo Canyon Power Plant (PGEC 2010) has similar source types. Due to a larger number of scenarios available for their study, we judged that their aleatory uncertainty estimates were more reliable. We adopted their aleatory uncertainty estimate for each source type as an upper bound upon our total aleatory uncertainty estimates. The upper bound for total aleatory uncertainty used for earthquake sources corresponds to a σ_{ln} value of 0.6. The upper bound for total aleatory uncertainty used for landslide sources correspond to a σ_{ln} value of 0.7.

2.5. Epistemic Uncertainty of Tsunami Waves

Epistemic uncertainties are calculated for the uncertainty in the distribution of the parameters to predict the hazard parameter of concern. Epistemic uncertainty is the uncertainty arising due to lack of knowledge, insufficient data, or available alternative models, and in concept, reduces as more data or information become available. Epistemic uncertainties may also be categorized into modelling and parametric uncertainties (Abrahamson et al. 1990). Some model parameters may be parsed as epistemic, and their (discrete) choices with weights would be included as additional branches in the logic tree. Epistemic uncertainties are generally discrete values and are combined using the logic tree method. Parameters such as slip rates, annual recurrence rates of events for individual sources, b-values of recurrence relationships, and alternative recurrence models are examples of parametric epistemic uncertainties included in the model.

While two different models were used in the context of deterministic modelling of the selected scenarios, the most credible or otherwise most conservative set of results were used, depending on the modelled tsunamigenic mechanism. If all scenarios of all source types were calculated using two alternative credible models, they could be included in the logic tree with weights, and would contribute to the modeling epistemic uncertainty.

3. Tsunami Source Regions and Scenarios

3.1. Tsunami Evidence In and Near the Bay of Fundy

The Point Lepreau Generating Station lies at an elevation higher than 13 m above mean sea level, on the northwestern side of the Bay of Fundy approximately 50 km from the mouth of the bay and 40 km south of Saint John, New Brunswick. No historical tsunamis have been recorded in the Bay of Fundy (NCEI 2014, accessed 2014) and paleoseismic studies did not interpret evidence for any tsunami above 2–4 m in the last 2350 years (Tuttle et al. 2014). The paleoseismic survey did interpret evidence of liquefaction indicating Holocene earthquakes in the area,

including potential Holocene activity on the Oak Bay fault approximately 45 km to the southwest of the site. Besides deposits of the 1929 Grand Banks tsunami (Tuttle et al. 2004; Moore et al. 2007), only one other potential tsunami deposit, a 2300-year-old layer in South Bay, New York, has been identified along the Atlantic coast of North America (Krentz 2009). If the deposit is related to a tsunami, the runup would have been 2–3 m.

The cumulative tsunami hazard of the Atlantic margin of North America is difficult to characterize due to both the variety of sources and the low recurrence rates. Many previous PTHA studies have focused on regions where the local subduction zones dominate the hazard such as sites on the Pacific Ocean, and have not considered landslides (e.g., Rikitake and Aida 1988; Geist and Parsons 2009; Annaka et al. 2007; González et al. 2009). Along the Atlantic margin, previous studies have not run inundation models but used a numerical function to relate deeper water wave height to run up (e.g., Grilli et al. 2009; Leonard et al. 2012).

The November 18, 1929 Grand Banks tsunami is the only large historical tsunami recorded on the Atlantic coast of Canada (NCEI 2014, accessed 2014; Fig. 1). A M 7.2 earthquake triggered a submarine landslide on the continental slope and generated wave runups of over 10 m (Ruffman 1997). Other tsunamis of note in the region were the 1755 Lisbon tsunami event which was observed in Newfoundland (Ruffman 2006) and recent global events such as the 2004 Indian Ocean tsunami (Thomson et al. 2007) which were recorded on tide gauges. None of these events were observed in the Bay of Fundy (NCEI 2014, accessed 2014).

3.2. Source Characterization

Both probabilistic and deterministic studies were conducted for the site. The sources were selected based on a literature review and previous studies for tsunami hazard in the northeast Atlantic Ocean.

3.3. Earthquake Sources

Local and transoceanic fault sources with the potential to generate tsunamis at the PLGS site were evaluated. Transatlantic convergent plate boundaries capable of generating tsunamis that could affect the site include the Azores-Gibraltar plate boundary (origin of the historic 1755 tsunami) and the Caribbean-North American plate boundary near the Puerto Rico trench (Fig. 1). The Oak Bay fault in the Bay of Fundy was considered as a potential local source because of its postulated Quaternary activity and proximity to the site. Earthquake source parameters used in the models are presented in Table 1.

3.3.1 Azores-Gibraltar Plate Boundary

On 1 November 1755, a magnitude 8.5–9 earthquake (e.g., Johnston 1996; Zitellini et al. 2001; Gutscher et al. 2006; Muir-Wood and Mignan 2009) off the coast of Lisbon, Portugal generated a large tsunami that caused damage on both sides of the Atlantic Ocean. The closest observation of the tsunami to the site was the draining and flooding of the Bonavista, Newfoundland harbor (Ruffman 2006). The Atlantic and Gulf of Mexico Tsunami Hazard Assessment Group (AGMTHAG 2008) hypothesize that bathymetric scattering of the tsunami energy or the great width of the continental shelf may have protected the east coast of the US from the 1755 tsunami. In contrast, bathymetry and fault orientation may have led to energy being focused toward Newfoundland and the Caribbean where the tsunami was observed. Other large historical earthquakes in the Azores-Gibraltar plate boundary region that generated tsunamis include a M 6.5 earthquake in 1722 (Baptista et al. 2006), two M 7.8 earthquakes in 1761 and 1969 (Johnston 1996), and a M 8.4 in 1941 (Buforn et al. 1988; Fukao, 1973).

Convergence at the Azores-Gibraltar plate boundary is distributed over a 200–300 km wide area (Grimison and Chen 1986; Hayward et al. 1999). Convergence of the plates is oblique at a rate of approximately 4–5 mm/year (Calais et al. 2003; DeMets et al. 2010). Of seven faults in the Azores-Gibraltar plate boundary area identified as potential sources for the 1755 earthquake (e.g., AGMTHAG 2008; Barkan et al. 2009; Grilli and Grilli 2013a), four were modeled in this study based on their orientation and resulting likelihood of generating a tsunami that could impact the Canadian Atlantic

Table 1

Fault source parameters used for tsunami modeling

Source area	Source ID	Earthquake magnitude (Mw)	Average slip (m)	Fault width (km)	Fault length (km)	Strike (°N)	Dip (deg)	Rake (deg)	Depth of fault plane centroid (km)	Shear modulus (kg/m s²)	Centroid latitude (deg N)	Centroid longitude (deg W)
Bay of Fundy	OBF1	7.0	1.5	22	55, 7.74	154, 134	85	45	10.96	2×10^{10}	45.09, 44.85	67.12, 66.92
	OBF2	6.5	0.3	22	55, 7.74	154, 134	85	45	10.96	2×10^{10}	45.09, 44.85	67.12, 66.92
Puerto Rico Trench	PRT1	9.0	15	95	550, 300	90, 115	20	60	21.25	3×10^{10}	19.36, 18.84	65.74, 62.10
	PRT2	9.1	20	95	550, 300	90, 115	20	60	21.25	3×10^{10}	19.36, 18.84	65.74, 62.10
	PRT3_TB	9.0	25 top, 5 bottom	47.5 × 2	550, 300	90, 115	20	60	13 top, 29 bottom	3×10^{10}	19.02 top, 18.66 bottom	62.01 top, 62.19 bottom
	PRT4	8.6	4	95	550, 300	90, 115	20	60	21.25	3×10^{10}	19.36, 18.84	65.74, 62.10
	PRT5	8.8	9	95	550, 300	90, 115	20	60	21.25	3×10^{10}	19.36, 18.84	65.74, 62.10
	PRT5A	8.7	9	95	550	90	20	60	21.25	3×10^{10}	19.36	65.74
	PRT5s	8.8	9	95	550, 300	90, 115	20	60	21.25	3×10^{10}	19.36, 18.84	65.74, 62.10
	PRT6	8.2	3.5	84	290	90	20	60	21.25	3×10^{10}	19.36	65.74
	NHF1	8.9	20	95	525	100	20	23	21.25	3×10^{10}	19.71	70.82
	NHF2	8.5	5	95	525	100	20	23	21.25	3×10^{10}	19.71	70.82
Iberia	GSZ1	9.1	20	210	200	350	40	90	72.49	6.5×10^{10}	35.38	7.76
	GSZ2	8.5	3	210	200	350	40	90	72.49	6.5×10^{10}	35.38	7.76
	GSZ3_TB	9.1	25 top, 15 bottom	105 × 2	200	350	40	90	20.27 top, 50.80 bottom	6.5×10^{10}	35.28 top, 35.34 bottom	8.43 top, 8.04 bottom
	GSZ4	8.7	15	80	200	350	40	90	25.71	6.5×10^{10}	35.38	7.76
	MPF1	8.8	20	80	200	20	40	90	25.71	6.5×10^{10}	37.37	9.37
	MPF2	8.5	7	80	200	20	40	90	25.71	6.5×10^{10}	37.37	9.37
	GBF1	8.7	13	80	200	60	40	90	25.71	6.5×10^{10}	37.06	10.84
	GBF2	8.5	7	80	200	60	40	90	25.71	6.5×10^{10}	37.06	10.84
	MTR1	8.7	13	80	200	10	40	90	25.71	6.5×10^{10}	37.64	14.93
	MTR2	8.5	7	80	200	10	40	90	25.71	6.5×10^{10}	37.64	14.93

coast: the Gibraltar subduction zone, the Marques de Pombal-Guadalquivir fault, the Gorringe Bank fault and the Madeira Tore Rise. A sensitivity study was performed to determine the impact from the largest plausible event (M 9.1) in this area. Because of the minimal tsunami runup at the site generated by M ~9 events on these faults, the faults were modeled as generalized straight line sources with a length of 200 km, a dip of 40 degrees, a rake of 90 degrees, and a width of 80 km. For the Azores-Gibraltar plate boundary, sources ranging from M 8.5 to M 9.1 were modelled. Because the slip rates on the individual sources in the Azores-Gibraltar plate boundary area are not well constrained, and because there is evidence of widespread paleotsunamis and turbidity currents in the region, we use the paleoseismic record to constrain the combined recurrence of earthquakes for the four sources modelled in this study. Based on the paleoseismic record (e.g., Luque et al. 2002; Scheffers and Kelletat 2005; Morales et al. 2008; Gràcia et al. 2010; Leonard et al. 2012) we assume 5–6 large magnitude (≥M 8.5) events in the past 9000 (±1000) years. The cumulative rate for M 8.5 and larger earthquakes is estimated using a Poisson model and follows the methodology of EPRI et al. (2012). The combined earthquake recurrence rate for the zone was is then divided among the four fault sources, with 50% of the rate assigned to the GSZ, 30% of the rate assigned to the MPF, and 10% of the rate assigned each to the GBF and MTR. The higher rates assigned to the GSZ and MPF are based on the evidence for Quaternary activity and the capability to generate large earthquakes on those structures (e.g., Zitellini et al. 2004; Thiebot and Gutscher 2006). Lower rates are given to the GBF and MTR because most of the deformation on the GBF appears to have occurred during the Miocene, and present activity is almost absent or not detectable in seismic data across the structure (Zitellini et al. 2004). The lower rate assigned to the MTR fault source also reflects the likelihood that this fault would likely produce strike-slip earthquakes with minimal vertical slip (e.g., Buforn et al. 1988; ten Brink et al. 2014), and its location to the west of the Madeira–Tore Rise may not allow for correlation with all events in the paleoseismic record described above. Mean recurrence intervals were estimated for ≥M 8.5

earthquakes in the Azores-Gibraltar plate boundary zone, at approximately 2500 years for the GSZ, 5000 years for the MPF, and 20,000 for the GBF and MTR.

3.3.2 Caribbean-North American Plate Boundary

Although no historical tsunamis associated with the Caribbean-North American plate boundary have impacted the Canadian Atlantic coast, the location (approximately 2800 km south of the site) and orientation of the plate boundary suggest that great earthquakes along this boundary could generate tsunamis at the site. The approximately east–west trend of the Puerto Rico trench (PRT) would result in tsunami energy being directed largely to the north toward the Canadian Atlantic coast. Global positioning system (GPS) measurements taken between 1994 and 2000, indicate that relative convergence of the North American Plate and Puerto Rico microplate is 17 ± 1 mm/year in a WNW direction (Jansma et al. 2000; Calais et al. 2002); this lies within the previous estimates of between 11 and 37 mm/year based on global tectonic models (Sykes et al. 1982; DeMets et al. 1990). DeMets et al. (2010) estimate the relative convergence rate between the North American and Caribbean plates at 19–21 mm/year. The motion along the PRSZ is largely left lateral with an estimated 3–6 mm/year of seismic slip along the subduction interface (LaForge and McCann 2005; DeMets et al. 2010). As a result of the highly oblique slip along the Puerto Rico subduction zone (PRT), frequent small to moderate earthquakes occur in the PRT region, and large subduction earthquakes are rare. The largest instrumentally recorded earthquake in the PRT area was a M 7.3 in 1943, although McCann (1985) suggests that an earthquake in 1787 was as large as M 8.0–8.25. Only six >M 7 earthquakes have been observed near the PRT in the last 220 years, with only two events >M 8; twelve >M 7 earthquakes were observed in the last 500 years (Grilli et al. 2010). At least four of the above earthquakes generated tsunamis. A M 7.8 earthquake ruptured an 80 km long section of the subduction zone in 1943 (Dolan and Wald 1998). Though the Puerto Rico trench has not experienced a historical great megathrust earthquake (M > 8),

similarities between its relative plate motion and that of the Sumatra–Andaman plate boundary has led to the hypothesis that M 8 + thrust earthquakes could happen there (AGMTHAG 2008). The North Hispaniola fault is the continuation of the North American-Caribbean plate boundary west of the Puerto Rico trench, and is also considered in the study.

Because of the potential impact of tsunamis generated at the Puerto Rico trench, variations in fault geometry, rupture length, and slip per event were considered in our model. We consider rupture lengths of 850, 550, and 290 km. The 850 km length rupture extends from the east end of the Northern Hispaniola fault to east end of the Greater Antilles subduction zone, and follows the fault geometry used in Gica et al. (2008). Potential tsunami scenarios have been modelled for earthquakes ranging from M 8.2 to M 9.1, originating in the Puerto Rico Trench and the North Hispaniola fault.

Recurrence rates of large earthquakes on the Puerto Rico trench are calculated assuming a 90% probability that the subduction zone is 20% coupled (e.g., Mueller et al. 2003; LaForge and McCann 2005; ten Brink et al. 2014) with a slip rate of 3.4 mm/year and a 10% probability that the subduction zone is accommodating the full convergence rate of 17 mm/year, to account for uncertainties in the degree of coupling. Accounting for the subduction not being fully coupled lowers the recurrence rate compared to other studies such as Geist and Parsons (2009) that assumed full coupling. The characteristic model of Youngs and Coppersmith (1985) is used to calculate recurrence. Recurrence rates for the PRT are estimated at one event in approximately 2800 years for M 8.5 earthquakes and one event in approximately 20,000 years for M 9.0 earthquakes.

3.3.3 Oak Bay Fault

The Oak Bay fault in the Bay of Fundy is considered to be potentially active and was assessed as the only potential local fault source in the Bay of Fundy. The Oak Bay fault (OBF) is an approximately 55 km long, oblique strike-slip fault that appears to control the west side of Passamaquoddy Bay (Fig. 2) and the trend of the St. Croix River channel (Gates 1989).

Although several investigations of geologic features in the region, both on land or beneath Passamaquoddy Bay, have failed to find evidence of Quaternary movement on the Oak Bay fault (Burke and Stringer 1993), Quaternary activity on the Oak Bay fault has been hypothesized based on pockmarks in Passamaquoddy Bay and historical seismicity in Passamaquoddy Bay. The Oak Bay fault is located mostly on land and in shallow water, which reduces its tsunami generation capabilities. Potential scenarios were modelled for M 6.5 and M 7.0 earthquakes. The recurrence rates for the Oak Bay fault have been estimated at approximately one event in 50,000 years for M 6.5 earthquakes and recurrence rates of greater than one event in 100,000 years for M 7.0 earthquakes.

3.4. Landslide Sources

Two types of landslides were considered in the hazard analysis—large failures from the flanks of the volcanic Canary Islands and failures along the continental slope that borders the Gulf of Maine. For this study, the term landslide is used to include all types of submarine mass failures including slumps, translational and rotational failures.

3.4.1 Continental Slope

With only one historical event, determining the recurrence and volume of landslides along the continental slope requires interpretation of the geological record. In addition to the 1929 landslide-generated tsunami event, landslide scars mapped by bathymetric surveys (Booth et al. 1993; McAdoo et al. 2000; Chaytor et al. 2009) and landslide deposits mapped in seismic lines (Giles et al. 2010; Huppertz et al. 2010; Piper et al. 2012) indicate that landslides have occurred along the continental margin of both the U.S. and Canadian Atlantic coast. Chaytor et al. (2009) mapped the landslide scars along the U.S. margin using multibeam swath bathymetry data compiled into a digital elevation model. The volume distribution of landslide scars mapped by Chaytor et al. (2009) is described as log-normal centered on a volume of 0.86 km^3. Although the U.S. margin is well mapped, few of the landslides

have been dated. In contrast, along the Canadian margin, studies using seismic data and sequence stratigraphy have calculated the recurrence of landslide events (Giles et al. 2010; Huppertz et al. 2010; Piper et al. 2012) but have more difficulty estimating the volume of the failures. Piper et al. (2012) interpreted seismic data to conclude large landslides (12–862 km^3) in slope environments similar to the one adjacent to the Gulf of Maine occur at a rate of approximately one event per 100 kyr for a 200 km stretch of continental slope.

To circumvent the low number of dated landslides for calculating recurrence, other studies (e.g., ten Brink et al. 2009; Grilli et al. 2009) have tied the landslide recurrence to earthquake recurrence. This methodology assumes that all large landslides are initiated by ground acceleration during an earthquake. We compared the landslide recurrence results of the methodology outlined by ten Brink et al. (2009) to a method that linked the recurrence of large landslides based on seismic data along the Canadian margin (Piper et al. 2012) to the landslide volume distribution from the U.S. margin (Chaytor et al. 2009). The recurrence based on the ten Brink et al. (2009) method used earthquake catalogs from EPRI et al. (2012) and the Geological Survey of Canada in two zones similar to the Atlantic highly extended crust and extended continental crust—Atlantic Margin zones from EPRI. The recurrence of landslides based on the ten Brink et al. (2009) method gave at least an order of magnitude lower landslide recurrence than the second method. Using the ten Brink et al. method, the recurrence of M 7.5 earthquakes within 100 km of the continental slope in the study area was approximately 870 kyr. The recurrence of the lowest magnitude considered capable of initiating a landslide (M 5.5) was over 50 kyr within in a 50 km buffer of the slope. The second method was chosen to represent landslide recurrence in this study to include the possibility that some landslides that generate tsunamis are not initiated by earthquakes.

We tied the recurrence of large landslides from Piper et al. (2012) to the volume distribution from Chaytor et al. (2009) at the 10 km^3 volume. The Poisson recurrence model used for the Azores-Gibraltar Plate Boundary sources was used to calculate an uncertainty distribution for the recurrence rate

of 10 km^3 and larger landslides. The hazard computation included the effect of landslides up to 200 km^3, a volume larger than mapped Quaternary events. The b-value distribution from Chaytor et al. (2009) was converted to a b-value appropriate for the mapping between landslide volume and magnitude. This b-value was used as a median. The discretized distribution of the b-value was calculated to be 0.489, 0.543, and 0.597 with weights of 0.2, 0.6 and 0.2, respectively.

We performed a sensitivity study with eight landslide sources spaced 100 km apart along the continental slope bordering the Gulf of Maine to determine both which sources posed the greatest threat to the study site and how distant of sources should be considered for the hazard assessment (Fig. 2). Bathymetric profiles of the continental slope were taken at each site to calculate slope. An additional site (6.5) was included between sources 6 and 7, at the mouth of the Northeast Channel adjacent to Georges Bank, which resulted in the highest runup at the site.

Based on mapped Quaternary landslide scars from along the U.S. and Canadian continental Atlantic margin (McAdoo et al. 2000; Fine et al. 2005; Chaytor et al. 2009, 2012; Lee 2009; Locat et al. 2009; Mosher and Campbell 2011; Piper et al. 2012; Locat et al. 2013), and the volume of the 1929 event (Mosher and Piper 2007a), 165 km^3 was used as the largest volume deterministic scenario. For the probabilistic scenarios, the volume and ratios of length, width and height were varied. Landslides were modeled as translational slides because this style of failure is several times more common than other styles in the region (Booth et al. 1993; McAdoo et al. 2000). In addition, translational slides may be more efficient at generating tsunamis than slumps (Grilli and Watts 2005); therefore, modelling translational slides is also the more conservative approach.

The overall characteristics, and largest plausible volume of the modelled hypothetical landslides of 165 km^3, were based on the prehistoric Currituck landslide (Geist et al. 2009; Locat et al. 2009; Grilli et al. 2013; Grilli et al. 2015). The largest slides considered had a length of 34 km, width of 22.67 km, and a maximum thickness of 410 m. The upper edge of the slides was assumed to be located at a depth of 500 m in all cases, while the depths of the

Table 2

Initial conditions for modeling the of landslide sources

Source ID	Landslide volume (km^3)	Direction (°N)	Slope incline (deg)	Bulk density (kg/m^3)	Thickness (m)	Length (km)	Width (km)	Depth (m)	Latitude (deg N)	Longitude (deg W)
TS1_H0	165	181	3.3	1900	410	34	22.67	1622	39.76	70.44
TS2_H0	165	163	2.7	1900	410	34	22.67	1809	39.79	69.23
TS3_H0	165	169	3.3	1900	410	34	22.67	1949	40.07	68.18
TS4_H0	165	146	2.8	1900	410	34	22.67	1947	40.36	67.05
TS5_H0	165	122	3.5	1900	410	34	22.67	1936	41.00	66.22
TS6_H0	165	111	2.5	1900	410	34	22.67	1772	41.71	65.53
TS7_H0	165	148	2.4	1900	410	34	22.67	1562	42.26	64.81
TS8_H0	165	152	1.7	1900	410	34	22.67	1116	42.63	63.80
TS6.5_H0	165	131	2.3	1900	410	34	22.67	1686	42.05	65.25
TS6.5_M0	10	131	4	1900	80	18.97	12.65	1163	42.09	65.32
TS6.5_L0	0.06	131	10	1900	20	3	2	1546	42.06	65.27

Depth, latitude and longitude are indicated for the top (center) of the landslide

centers of the slides were computed based on the slope at each of the hypothesized slide locations. The average slope over the conceptualized tsunamigenic portion of the slide motion was measured along each transect over the distance equivalent to the length of the slide in the direction of motion. The maximum initial amplitudes estimated using the semi-empirical model by Grilli et al. (2011) for the high volume cases range from 27.4 m to 49.8 m among the different locations. Since the slide dimensions and the depth of the upper edge of the slide are the same across all nine locations considered, the differences in the initial amplitudes are largely due to the variations in slope angles at the different locations. To calculate variability for the probabilistic portion of the study, two other scenarios were modelled— volumes of 10 and 0.06 km^3, with the 10 km^3 landslide representing the low end of the volume range for large, infrequent landslides along the Canadian margin (Piper et al. 2012) and 0.06 km^3 representing the 5th percentile of the range of the lognormal calculation and was used as the cutoff for exceedance computation. Initial landslide parameters are presented in Table 2. Further details on the submarine landslide tsunami generation process are presented later in the Source Modelling section.

3.4.2 Canary Islands

The tsunamigenic potential of large (up to 500 km^3) failures off the flanks of the Canary Islands and specifically the most active volcano in the chain, Cumbre Vieja (CVV) on the island of La Palma, was studied first by Ward and Day (2001). Since that time, several studies have challenged some of the assumptions presented in the in the original study including the volume of the failure and the formulas used to model transatlantic wave dispersion (Mader 2001; Pararas-Carayannis 2002; Wynn and Masson 2003; Løvholt et al. 2008; Abadie et al. 2012; Hunt 2012). For this study we based the volume and recurrence of landslides on the recent turbidite work by Hunt et al. (2013, 2014). Evidence based on turbidites in the Madeira Abyssal Plain and Agadir Basin indicate that the large landslide scars mapped on the Canary Islands failed in a series of retrogressive landslides ranging from approximately 10–100 km^3 (Hunt et al. 2013). This is similar to the largest plausible scenario of 80 km^3 of Abadie et al. (2012) for Cumbre Vieja based on geotechnical assessments. Based on the 1.5 Myr record from the western Canary Islands, the recurrence of major landslides in the island group is ~1/100 kyr and for an individual island 1/300 kyr (Hunt et al. 2013). Analysis of a longer record by Hunt et al. (2014) produced similar results by documenting 125 turbidites originating in the Canary Islands during the last 17 Ma (~130 to 135 kyr recurrence).

The potential range of landslide volumes for the Canary Islands was considered to be 10–125 km^3 with a recurrence of landslide events of approximately 100 kyr for the island chain and 300 kyr for

each of the three most volcanically active islands (La Palma, Tenerife and El Hierro) turbidite record for the past 1.5 Myr. The maximum possible subevent volume is estimated to be slightly higher based on the estimated average size (125 km^3) of subevents of the Roques de García landslide, which has a mapped volume of 500 km^3 and 4 subevents (Hunt et al. 2013). As the most volcanically active island, La Palma was considered to be the most likely source of future events. Deterministic landslide sources of 80, 40, and 20 km^3 based on the initial tsunami conditions modeled by Abadie et al. (2012) were used as the deterministic sources for this study. Abadie et al. (2012) also studied a 450 km^3 scenario as an extreme case; however, this case was considered extremely unlikely, and was not included in the probabilistic hazard assessment.

Because large landslides in the Canary Islands are linked to periodic episodes of volcanic activity (Hunt et al. 2014), the Poisson model, which assesses recurrence based on only the average rate of events, may not accurately model recurrence. The Brownian Passage Time (BPT) model developed by Matthews et al. (2002), accounts for steady-state loading with periodic events was determined to be more appropriate for the geological conditions that lead to slope failures in the Canary Islands. Poisson and Brownian Passage Time models were given equal weigh in the hazard assessment. The most recent landslide was 15 ka on the island of El Hierro (Masson et al. 2002; Hunt et al. 2013), therefore, based on the BPT analysis El Hierro has a lower calculated recurrence rate leading to the lower contribution to the hazard than La Palma and Tenerife.

3.5. Source Modelling

3.5.1 Coseismic Source Modelling

The initial coseismic deformation for the selected earthquake sources was computed using the standard model developed by Okada (1985), assuming uniform material properties in an elastic half-space medium defined by the Poisson's ratio ($v = 0.25$). The model provides an analytical solution for the sea floor deformation based on earthquake location, fault plane geometry, and moment magnitude. In the framework of the source model, the total energy released by an earthquake is a function of the shear modulus μ, the fault area A, and the slip distance Δ:

$$M_0 = \mu \bar{\Delta} A \tag{11}$$

The earthquake magnitude is then related to the total energy as follows:

$$M_w = (\log M_0)/1.51 - 6.07. \tag{12}$$

Furthermore, it was assumed that the coseismic displacement occurs instantaneously, and that the sea surface elevation is equivalent to the sea floor deformation.

3.5.2 Continental Slope Landslide Source Modelling

The initial tsunami conditions associated with the hypothesized submarine landslides on the continental shelf slopes of New England and the Scotian Shelf were estimated through the semi-empirical model by Grilli et al. (2011). In their framework, the landslides are conceptualized as rigid semi-elliptical masses sliding down a plane with a constant slope. The model formulations are based on the numerical modelling of slide kinematics by Grilli and Watts (1999, 2005), Grilli et al. (2002), Watts and Grilli (2003), Watts et al. (2003, 2005), as well as the laboratory experiments of rigid underwater slides of Enet et al. (2003), Enet and Grilli (2005, 2007). The source model has been applied in a number of historical case studies aiming to reproduce the source mechanism or observed tsunami wave heights (Tappin et al. 2008; Day et al. 2005; Watts et al. 2005).

The landslide kinematics during the tsunamigenic phase of the motion is quantified in terms of the idealized slide and slope configuration. The modelling and scaling analyses by Grilli and Watts (2005) indicated that the key parameter in submarine landslide tsunami generation is the initial acceleration, and the rigid body assumption neglects any effects of the landslide deformation on the tsunami generation process. The initial tsunami waveform is approximated by the sum of two Gaussian functions in the direction of slide motion, with a characteristic depression wave on the shoreward side, and a positive elevation wave on the offshore side. The initial velocities generated during the slide motion are

specified based on the depth-integrated mass conservation for long waves (Grilli 1997; Grilli et al. 2011).

3.5.3 CVV Source Modelling

The initial water levels and velocity fields used to model the Cumbre Vieja Volcano subaerial landslides were generated by Abadie et al. (2012), and graciously shared by Abadie (pers. comm., 2014) and Harris (pers. comm., 2015). They modeled the initial conditions using an incompressible version of a multiple-fluid/material Navier–Stokes model (THE-TIS-3D) for four potential slide volumes of 20, 40, 80, and 450 km^3. These scenarios have also been used for tsunami hazard assessment within the U.S. East Coast NTHMP (Grilli and Grilli 2013b; Tehrani-rad et al. 2015).

3.6. Propagation and Inundation Modelling

3.6.1 Transatlantic propagation and inundation modeling

The transatlantic propagation and inundation of the tsunami scenarios from the GSZ, PRT and CVV source regions was modelled using the Delft3D model (Apotsos et al. 2011; Vatvani 2005; van Veen et al. 2014), which is based on the non-linear shallow water equations, discretized on a staggered Arakawa C-grid. The model was implemented on spherical coordinate grids with progressively increasing resolution, connected either through one-way nesting (on the continental shelf and shelf slope) or through a two-way domain decomposition scheme (near the site, within the Bay of Fundy). Two different spatial discretization schemes were used for the advective terms: the default, Cyclic scheme (Stelling and Leendertse 1992) was used for the domains covering the Atlantic Ocean, the continental shelf, and most of the Bay of Fundy; the fine resolution domains within a few kilometres of the site used the Flooding scheme (Stelling and Duinmeijer 2003), which is capable of representing rapidly varying flows for a wide range of Froude numbers. In the Cyclic scheme, the advection terms are integrated implicitly in time, allowing for a less strict definition of the time step. The advection terms in the Flooding scheme are integrated explicitly through time, and the time step is restricted by the Courant number for advection.

The tsunami propagation and inundation was resolved through five levels of nested and linked grids increasingly higher resolution: from 2′ (~3.6 km) for most of the Atlantic Ocean, 15″ (~500 m) for the continental shelf, 7.5″ (~250 m) for the Bay of Fundy, to 2.5″ and 1″ (~83 and ~28 m) in the vicinity of the PLGS (Table 3). Each scenario has been modeled at a nominal initial still water level corresponding to mean sea level (MSL), and additionally with the tide level set at the highest astronomical tide (HAT) of +4 m above MSL at Pt. Lepreau, to evaluate the sensitivity of tsunami runup to the stage of the tide. The Oak Bay fault scenarios originating in Passamaquoddy Bay were initialized directly in the Bay of Fundy grid and the two finer grids.

The bathymetry and topography in the modelling grids were generated from several overlapping datasets, including a high resolution survey of Point Lepreau Peninsula; topographic datasets from the GeoNB database (Service New Brunswick 2014); the Gulf of Maine bathymetry and topography composite dataset including full coverage of the Bay of Fundy; and finally, the global GEBCO_08 bathymetry and topography dataset at 30″ horizontal resolution by the British Oceanographic Data Centre (BODC 2014). The propagation of tsunami generated by submarine

Table 3

Deterministic modelling grid spacing for all domains

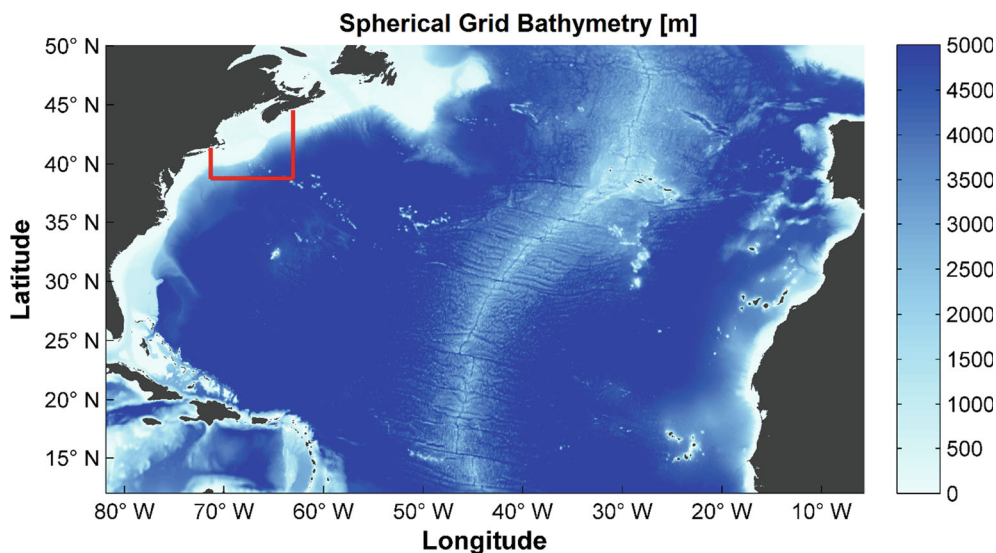| Model domain	Spherical grid resolution	Cartesian grid resolution
Atlantic Ocean	2′	N/A
Regional (Gulf of Maine, Scotian Shelf)	15″	501 m
Bay of Fundy	7.5″	250.5 m
Approach to Point Lepreau	2.5″	83.5 m
Point Lepreau peninsula	0.83″	27.83 m

Figure 3
Bathymetry of the Atlantic Ocean modeling grid (2′ resolution). The boundaries of the nested regional continental shelf grid (15″ resolution) are marked in *red*
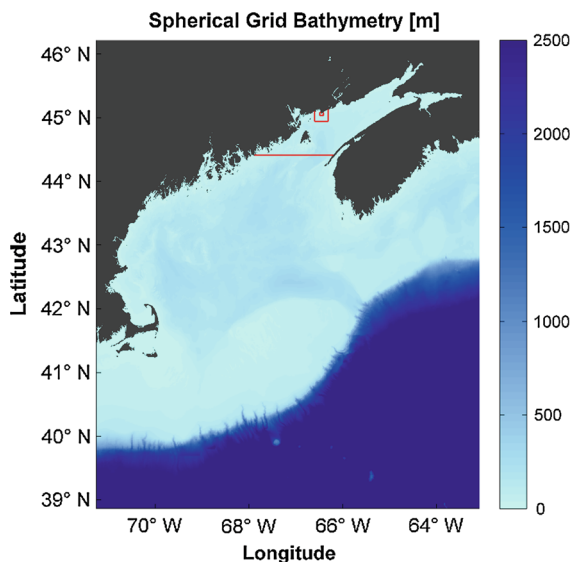

Figure 4
Bathymetry of the regional continental shelf grid in spherical coordinates (15″ resolution), encompassing the continental shelf slope, Georges Bank, the Gulf of Maine and the Bay of Fundy. The boundaries of the nested Bay of Fundy (7.5″) and higher resolution coastal grids (2.5″ and 0.83″) are marked in *red*. The higher resolution grids are centered on the Point Lepreau peninsula in New Brunswick

landslides on the continental shelf was modelled on four levels of grids placed in UTM 19 coordinates, starting with a regional grid (Fig. 3) with a resolution

of 501 m. The boundaries of the nested grids covering the Bay of Fundy (resolution of 250.5 m), as well as the two finer grids (83.5, and 27.83 m near PLGS), were positioned similarly to those for the spherical coordinate grids (Fig. 4; Table 3).

To minimize the outgoing wave reflection from the outer boundaries of the coarsest grid, weakly reflective Riemann boundary conditions were pre-scribed on the open boundaries of the Atlantic grid for the transatlantic propagation cases, and on the open boundary of the Bay of Fundy grid in the Oak Bay fault scenarios. A standard value of the Manning friction coefficient of 0.02 s/m$^{1/3}$ was used in all Delft3D simulations. The 32-bit Delft3D suite version 4.01.00 was implemented in a 64-bit Windows environment.

3.6.2 Regional Landslide Propagation and Inundation Modeling

The propagation and inundation of the tsunami induced by the hypothesized continental slope land-slide events were modeled using the Cartesian coordinate version of the FUNWAVE-TVD model, utilizing the fully nonlinear Boussinesq equations, and a combined finite-volume and finite difference

MUSCL-TVD scheme (Chen 2006; Shi et al. 2012; Kirby et al. 2013). The FUNWAVE-TVD model has been applied in a range of tsunami case studies for both landslide and earthquake-generated events (Watts et al. 2003; Day et al. 2005; Grilli et al. 2007; Ioualalen et al. 2007; Tappin et al. 2008; Grilli et al. 2010, 2013b; Abadie et al. 2012; Harris et al. 2012). The benefit of using a fully nonlinear Boussinesq model over NSW models is that it has the capability to represent frequency dispersion processes, which is particularly important for the simulation of landslide-generated tsunami which are generally shorter and more dispersive than coseismic tsunami. The model has been validated for use in the U.S. NTHMP tsunami hazard mapping efforts using benchmark tests in Cartesian (Shi et al. 2012b; Tehranirad et al. 2013) and spherical coordinates (Tehranirad et al. 2012).

In the model version implemented for modelling submarine landslide tsunami in the present study (FUNWAVE-TVD 2.1), only the Cartesian coordinate formulations contain the full set of nonlinear terms, whereas the spherical coordinate formulations are only weakly nonlinear. Therefore, the effects of the earth's sphericity, including the Coriolis effect, are not accounted for in the Cartesian implementation on the regional grid used for submarine landslide tsunami originating on the continental shelf. Refinements in grid resolution in both versions of the FUNWAVE-TVD model are implemented through one-way nesting. To minimize the reflection of outgoing waves through the open boundaries of the coarsest grids, the outermost grid cells are assigned as sponge layers, typically with widths on the order of 100 km. The standard value of bottom friction coefficient of $C_d = 0.0025$ was used for all FUN-WAVE-TVD simulations following Grilli et al. (2013a). The FUNWAVE-TVD 2.1 model was implemented in a 64-bit Linux cluster environment, and was run in parallel mode using up to 32 processors.

4. Results and Discussion

Deterministic modeling of the probable maximum tsunami for all sources, combined with the mean annual maximum tide (labeled Higher High Water Large Tide, or HHWLT) of 3.8 m above MSL, range from 4.1 m for the Oak Bay fault, 4.6 m for the Iberia sources, 6.3 m for the Puerto Rico trench sources, 7.2 m for the Canary Island volcano scenarios, and 8.3 m for the continental slope landslides.

The potential flank collapse of the Cumbre Vieja Volcano, and the continental slope landslides are predicted to produce the highest runup at the site; however, they contribute less to the near-term hazard due to the relatively longer recurrence intervals (greater than 100 kyr) compared to those for large earthquakes (hundreds to thousands of years). For the landslide-induced tsunami hazard, the hypothesized continental slope landslides dominate the hazard except for low runup values (under 1 m), where the Canary Island sources are dominant contributors. For the drawdown landslide hazard, the Canary Island sources are dominant contributors to the landslide hazard till a drawdown level of about 2.5–3 m. At a return period of 10,000 years, the earthquake sources are the dominant source type contributing to the hazard, and the PRT is the dominant individual source contributor to the hazard. The runup hazard computed for the Highest Astronomical Tide level scenarios indicate runup values above the tide of 1.9 m for a return interval of 10,000 years, and 3.7 m for 100,000 years. The drawdown hazard computed for the MSL scenarios indicate drawdown values of 1.8 m below the tide for a return interval of 10,000 years, and 3.5 m below the tide for 100,000 years.

The probabilistic assessment also estimated the combined tide, runup and drawdown hazard by considering the annual exceedance levels for the tidal water levels. For the combined tidal and tsunami hazard for wave runup, the return period for a combined +4 m level above MSL, including high tides, is about 14,500 years, while for the combined hazard for wave drawdown, the return period for a combined −4 m level below MSL, including low tides, is about 24,000 years.

4.1. Coseismic Scenario Results

The results for the earthquake-generated tsunami scenarios are listed in Table 4, while the results for

Table 4

Deterministic modelling water level statistics for the earthquake-induced tsunami scenarios

Source area	Source ID	Earthquake magnitude (M_w)	Max initial amplitude (m)	All water levels are in meters (m) Referenced to mean sea level (MSL)			
				@ MSL: max runup	@ MSL: max drawdown	@ HHWLT: highest water level	@LLWLT: lowest water level
Bay of	OBF1	7.0	0.3	0.2	−0.2	4.1	−4.0
Fundy	OBF2	6.5	0.1	0.0	0.0	3.9	−3.9
Puerto Rico	PRT1	9.0	6.4	1.4	−1.4	5.4	−5.5
Trench	PRT2	9.1	8.5	1.7	−2.2	6.3	−6.3
	PRT3_TB	9.0	10.1	1.9	−3.2	6.3	−7.1
	PRT4	8.6	1.7	0.7	−0.6	4.7	−4.5
	PRT5	8.8	3.8	1.2	−1.1	5.0	−5.0
	PRT5A	8.7	3.7	1.2	−1.0	5.3	−5.2
	PRT5s	8.8	3.9	1.2	−1.1	5.0	−5.0
	PRT6	8.2	1.5	0.6	−0.4	4.4	−4.3
	NHF1	8.9	6.9	0.6	−0.5	4.5	−4.4
	NHF2	8.5	1.7	0.2	−0.1	4.1	−4.0
Iberia	GSZ1	9.1	12.2	0.3	−0.4	4.3	−4.1
	GSZ2	8.5	1.8	0.1	−0.1	3.9	−3.9
	GSZ3_TB	9.1	18.9	0.8	−0.6	4.6	−4.6
	GSZ4	8.7	8.2	0.2	−0.2	4.1	−4.1
	MPF1	8.8	10.9	0.4	−0.5	4.3	−4.2
	MPF2	8.5	3.8	0.2	−0.2	4.1	−4.1
	GBF1	8.7	7.1	0.2	−0.3	4.1	−4.1
	GBF2	8.5	3.8	0.1	−0.1	4.0	−4.1
	MTR1	8.7	7.1	0.4	−0.4	4.3	−4.2
	MTR2	8.5	3.8	0.3	−0.2	4.1	−4.1

Highest water level values include the runup modelled at HAT, superimposed with the HHWLT (mean annual maximum tide) level

the CVV and continental slope scenarios are summarized in Table 5. All water level values are referenced to MSL. The highest water levels reported at the HHWLT (Higher High Water Large Tide) datum are based on the addition of the runup modelled at the highest astronomical tides, and a stillwater level of 3.8 m corresponding to the HHWLT tidal level. The lowest water levels at LLWLT (Lower Low Water Large Tides) are based on the drawdown calculated for the mean sea level scenarios, and an added stillwater level of −3.8 m corresponding to the LLWLT datum. The HHWLT and LLWLT datums represent the mean annual maximum and minimum tides, respectively, computed from tidal predictions over 19 consecutive years.

The tsunamis originating in the Azores-Gibraltar Plate Boundary area took approximately 8 h to reach the continental shelf south of the PLGS site, and about 9.5 h to reach Point Lepreau. The scenarios from this source area produced the lowest overall impact at the site, with runup values in the range of 0.1–0.8 m. The highest impact was predicted due to the GSZ3_TB scenario (M 9.1) that represents the highest magnitude event from this source area, and is based on a source with a conservative slip distribution that produced 55% higher initial tsunami heights than the comparable GSZ1 (M 9.1) scenario.

Tsunami originating in the Northeast Caribbean Region traveled for approximately 4 h before reaching the continental shelf, and 5.5 h before reaching the coastline near the PLGS. The scenarios from this source area had the highest overall impact among the coseismic tsunami events, particularly the tsunami generated by earthquakes at the PRT fault. Runup values range from 0.3 m (NHF2, M 8.5) to 2.5 m (PRT3_TB, M 9.0) at high tide, and 0.2–1.9 m at mean sea level for the equivalent scenarios. Drawdown values range from −0.2 m (NHF2, M 8.5) to −3.3 m (PRT3_TB, M 9.0) for the HAT cases, and −0.1 to −3.2 m for the MSL cases, with drawdown values generally being less sensitive to the tidal stage

Table 5

Deterministic modelling water level statistics for the Cumbre Vieja Volcano (CVV) landslides, and continental shelf translational slides (TS)

Source area	Source ID	Landslide volume (km³)	Max initial amplitude (m)	All water levels are in meters (m) Referenced to mean sea level (MSL)			
				@ MSL: max runup	@ MSL: max drawdown	@ HHWLT: highest water level	@LLWLT: lowest water level
Canary Islands	CVV80	80	52.5	2.8	−3.4	7.2	−7.2
	CVV40	40	38.4	2.6	−3.0	6.6	−6.8
	CVV20	20	19.2	1.8	−2.2	5.9	−6.0
	CVV450[a]	450	116.6	4.3[a]	−5.4[a]	8.4[a]	−9.23[a]
Continental Slope	TS1_H0	165	49.8	0.8	−0.4	4.6	−4.2
	TS2_H0	165	31.5	2.0	−0.9	6.0	−4.7
	TS3_H0	165	38.0	1.8	−0.9	5.6	−4.7
	TS4_H0	165	29.6	2.9	−1.9	7.0	−5.7
	TS5_H0	165	41.8	2.1	−2.1	6.4	−5.9
	TS6_H0	165	28.9	2.6	−2.4	6.4	−6.2
	TS7_H0	165	33.2	2.9	−3.0	7.8	−6.8
	TS8_H0	165	33.2	3.0	−2.8	6.9	−6.6
	TS6.5_H0	165	27.4	3.2	−2.3	8.3	−6.1
	TS6.5_M0	10	8.8	0.9	−0.9	4.9	−4.7
	TS6.5_L0	0.06	0.3	0.1	0.0	3.9	−3.8

Highest water level values include the runup modelled at HAT, superimposed with the HHWLT (mean annual maximum tide) level

[a] The 450 km³ extreme volume scenario for the Cumbre Vieja Volcano is not considered to be plausible, and its contribution to the tsunami hazard levels is not included in the PTHA

than the runup values. The highest impact scenario was PRT3_TB, based on a source with a conservative slip distribution (most of the slip is distributed on the top half of the fault), but the same magnitude as the PRT1 source. The effect of the conservative slip distribution was an increase of 35–50% in runup height compared to the uniform slip source. Significant wave height amplification is predicted on the continental slopes and shallow areas such as the Georges Bank (Fig. 5), where a significant part of the wave energy is dissipated before the waves reach the shores of Maine and New Brunswick. The maximum heights of the waves reaching Point Lepreau peninsula in the PRT3_TB scenario are in the range of 0.5–1 m (Fig. 5). The maximum runup value of 2.5 m (above the tide) near the PLGS site is reached through amplification within Indian Cove, southwest of the site. The amplification factor based on the wave height at the mouth of Indian Cove is on the order of 2–2.5.

The OBF1 (M 7.0) scenario produces very small runup heights near the site (0.3 m at HAT, 0.2 m at MSL), and a drawdown of a similar magnitude (−0.2 m). The lower magnitude event OBF2 (M 6.5) results in negligible runup and

drawdown (magnitudes of <0.05 m at MSL, 0.1 m at HAT).

4.2. Continental Slope Scenario Results

The results for the landslide-generated tsunami scenarios are listed for all source locations, along with the maximum initial tsunami amplitudes in Table 5. Runup values above stillwater level range from 0.8 m (TS1_H0) to 4.5 m (TS6.5_H0) at high tide, and 0.8 m to 3.2 m at mean sea level. Drawdown values range from −0.4 to −3.3 at high tide, and −0.4 to −3.0 at mean sea level.

The highest runup near the PLGS site of 4.5 m (highest water level of 8.3 m above MSL, if occurring at HHWLT) is predicted for the highest volume landslide at location 6.5, which is positioned directly adjacent to the Northeast Channel (northeast of Georges Bank), and moving along a transect that is roughly aligned with the channel. Even for the landslide locations with the most favorable orientation (failure directly away from site) such as 6.5, 2 and 3, the runup is approximately an order of magnitude lower than the initial deformation (Fig. 2; Table 5). This is likely due to the wide
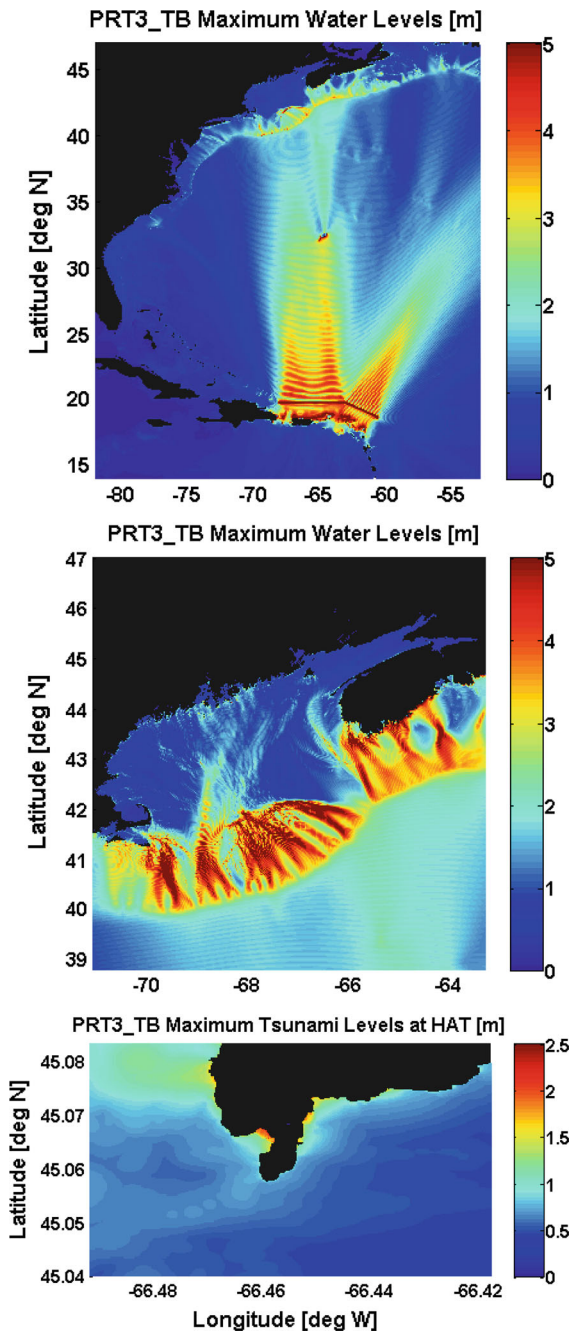
PRT3_TB Maximum Water Levels [m]

PRT3_TB Maximum Water Levels [m]

PRT3_TB Maximum Tsunami Levels at HAT [m]

Figure 5
Snapshots of maximum water levels captured throughout the simulation of the PRT3_TB event
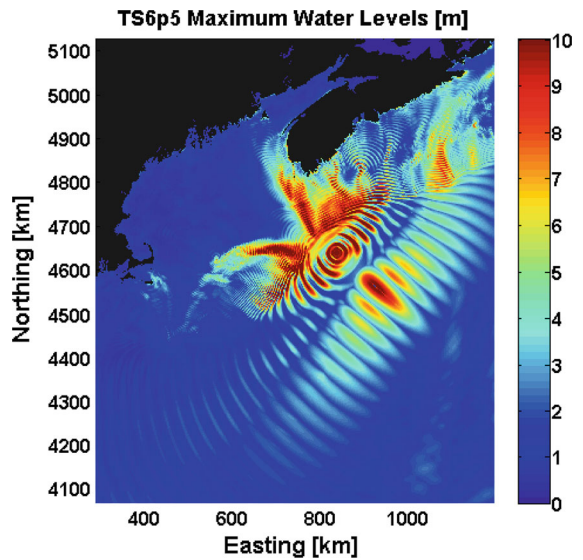
TS6p5 Maximum Water Levels [m]

Figure 6
Snapshots of maximum tsunami heights, captured at 3 min intervals throughout the simulation, for the high volume submarine landslide originating from location 6.5

shallow continental shelf of the Gulf of Maine and the Grand Manan Island and the southern tip of Nova Scotia dissipating wave energy.

For the highest volume landslide originating at location 6.5, the leading depression wave propagates along the Northwest Channel and expands within the Gulf of Maine, with the eastern front of the leading wave refracting toward the Bay of Fundy, and reaching the site after approximately 2.5 h. Overall the tsunami impact near the PLGS site is higher for locations 5–8 positioned along the east side of the continental slope adjacent to the Gulf of Maine, whereas locations 1–4 produce lower runup and drawdown values. This is in great part due to wave energy dissipation and refraction over the shallow Georges Bank, which likely diminishes the impact of the leading waves originating from those locations. The map of maximum tsunami heights for TS6.5_H0 (Fig. 6) shows that significant wave amplification occurs over the shallow banks, and the wave heights are largely attenuated by the time they reach the coastlines of Maine and New Brunswick, which can be attributed to dissipation by bottom friction (Tehranirad et al. 2015). In this case, the highest wave heights on the New Brunswick coastline are seen near Grand Manan Island and the adjacent shallow areas, which present a partial barrier in the path of the incoming waves to the PLGS location.

4.3. CVV Scenario Results

The tsunami waves generated by the Cumbre Vieja Volcano flank collapse (source modelled by Abadie et al. 2012) propagate in all directions, with the leading elevation wave traveling to the continental shelf near the Grand Banks in approximately 7 h, and to the Point Lepreau coastline in about 8.5 h. The wave trains from the three modelled scenarios generally exhibit similar propagation patterns, due to the fact that the initial wave trains following generation are quite similar in wavelength, period and orientation.

The tsunami amplitudes in the region near the PLGS site computed by Delft3D are consistently higher than the equivalent scenarios computed by Tehranirad et al. (2015) using the spherical coordinate version of FUNWAVE-TVD, by roughly a factor of two. Maximum runup near the PLGS site for the highest plausible slide of 80 km^3 (CVV80) is 3.4 m at high tide (maximum water level of 7.2 m if occurring at HHWLT), and 2.8 m at mean sea level as computed by Delft3D.

The discrepancy between the hydrodynamic model results in this study, compared to those of Tehranirad et al. (2015) derived for otherwise identical initial conditions can be attributed to the dispersive nature of the relatively short waveforms generated by the subaerial landslide, whose frequency dispersion and dissipation is likely more accurately described by the additional dispersive terms present in the FUNWAVE-TVD formulations. Due to the lack of frequency dispersion terms in Delft3D, a larger portion of the wave energy is propagated across the Atlantic Ocean and to the Canadian east coast. While the approach of using Delft3D for the CVV scenarios is likely overly conservative to be used generally in the context of the deterministic modelling of a single subaerial slide event, the lack of a robust historical validation case study for a massive volcano flank collapse or a larger number of identified plausible source mechanisms in this source region make it difficult to ascertain that the results are unreasonably conservative in the context of the PTHA. The use of the more conservative modelling approach accounts for some of the uncertainty introduced by our use of CVV collapse scenarios as proxy events for a wider range of possible subaerial landslides on the Canary Islands, some of which may produce wave trains that are less dispersive than the CVV events modelled by Abadie et al. (2012).

Compared to other PTHA in the region, our study had similar results although lower runups, likely due to the protected location within the Bay of Fundy. For landslide sources, in the Leonard et al. (2012) tsunami hazard study for the Canadian coastlines, the Bay of Fundy was lumped in with other outer Atlantic Ocean facing sources including Nova Scotia and southern Newfoundland. Looking at wave heights greater than 3 m, Leonard et al. (2012) calculated a recurrence interval of 114 kyr for continental slope landslides and 313 kyr for Canary Islands tsunamis. This is similar to our calculated recurrence of 250 kyr for continental slope and 500 kyr for Canary Island landslide tsunamis greater than 3 m. Grilli et al. (2009) determined at the 500-year recurrence interval some coastal sites had runup exceeding 3–4 m from submarine landslides, though most were between 1 and 2 m. For a runup from continental slope landslide sources exceeding 1 m a year the recurrence from this study is approximately 30 kyr. The lower rates for our site would be expected given its protected location on the Bay of Fundy and the wider continental shelf across the Gulf of Maine that other sites that are in the Leonard et al. (2012) and Grilli et al. (2009) studies. In addition, Grilli et al. (2009) employed a Monte Carlo simulation to account for variation in landslide parameters and some of the difference in results may be due to differences in the assumptions between their model and the one presented here including but not limited to Grilli et al. (2009) using a wider variety of landslide sources with an earthquake trigger and this studies propagation of the tsunami from source to site and use of the geological record for landslide recurrence.

4.4. Scaling Relationships Using Linear Regression

For any probabilistic hazard model, an important input is the specification of the hazard parameter of concern as a function of appropriate dependent parameters. In the PTHA, this translates to specification of amplitude of the wave runup or drawdown.

We have developed this specification of wave amplitude using the concepts similar to those employed for the probabilistic characterization of ground motions in PSHAs. Thus, the specification of wave amplitudes includes two necessary components. One component is a relationship for natural log of median peak wave amplitudes as a function of earthquake magnitude for earthquake sources or a function of natural log of landslide volume in km^3 for landslide sources. We generally use the term scaling relationship for this component. The other component is the specification of aleatory uncertainty (random variation) of wave amplitudes about the median amplitude. This component and its sub-components were described above in the aleatory uncertainty section.

Scaling relationships for all sources are computed using linear regression and variance statistics. As mentioned above, for earthquake sources, the regression is carried out with peak wave amplitudes (runup and drawdown) in natural logarithmic space and earthquake magnitude in real space. For landslide sources, the regression is carried out with peak wave amplitudes (runup and drawdown) in natural logarithmic space and landslide volume (in km^3 units) in natural logarithmic space. For drawdown, the absolute values of the peak wave amplitudes are considered in the regression.

A limited number of deterministic scenarios were explored in a 2-stage scenario selection process to determine the relative contribution to hazard from each source. Since regressions for all sources were based on this limited data, assumptions were made on a source-by-source basis to obtain usable scaling relationships. For each source group, linear regression parameters (α the intercept, and β the slope) were developed for the dominant source within the group (such as Puerto Rico Trench within the Caribbean-American plate boundary, and the Gibraltar Subduction Zone within the Azores-Gibraltar plate boundary). The components of the aleatory uncertainty (parametric, modeling and regression) and total aleatory uncertainty were computed for this dominant source, while applying appropriate upper bounds as explained in the aleatory uncertainty section. All other sources within a group used a scaling relationship formed by the equation of line

passing through two points, as these non-dominant sources had two computed scenarios each. The slope and intercept (α and β) were computed from these line equations. The aleatory uncertainty of the dominant source was applied to all sources within the group. For the Oak Bay fault, where only one source exists within the group, the total aleatory uncertainty of the Puerto Rico Trench was applied to the source.

Separate scaling relationships were developed for the HAT and the MSL tidal levels, and for runup and drawdown hazard computations. A lognormal probability distribution was applied to aleatory uncertainty for all sources.

For some sources, based on the computation results, the above described method of scaling relationships had to be amended. Such amendments are described below for any applicable sources.

4.4.1 Puerto Rico Trench (PRT)

Since the PRT produces the highest relative amplitude impact at the site among earthquake sources, and upon observing higher results for the PRT western segment scenarios for lower magnitude ranges (M 8.7 and below), we decided to incorporate location uncertainty for the PRT. To develop scaling relationships for the PRT, we first divided the earthquake magnitude into high magnitude ($\geq$M 8.8) and low magnitude ($\leq$M 8.7). For the high magnitude range, no location uncertainty was applicable due to long rupture lengths—hence the fault consists of a single segment (PRTH). For the low magnitude range, we applied location uncertainty by creating two segments, a western segment (PRT_LW) comprising 60 percent of the fault beginning from the westerly end, and an eastern segment (PRT_LE) comprising of the remaining 40 percent of the eastern extent of the fault.

For the PRTH and PRT_LE, regression was carried out using data from 4 scenarios initially, for both the HAT and MSL cases. Due to the low number of data points available and the observation that the regression parameters of both cases are in close range, we carried out a significance testing using the F test. The testing showed insufficient evidence for using different slopes. As a result, the combined eight

cases (4 from each case) were used for a single slope calculation. Separate intercepts (α) were computed for each case (HAT and MSL) using the common slope (β) value. These results were applied to the PRTH and PRT_LE.

Two scenarios of the western segment (PRT_LW) were used, and the equation that passes through both scenario points was used as the scaling relationship. Separate equations were developed for HAT and MSL cases.

For runup hazard, aleatory uncertainty computations were performed for both the HAT and MSL cases. The MSL case produced lower estimates, and in light of limited data and the high contribution of PRT to the hazard, we judged that we had limited support to apply the lower uncertainty to the MSL case. Hence, for the PRT, for runup hazard, we apply the larger aleatory uncertainty estimated from the HAT case to the MSL case. For drawdown hazard, the aleatory uncertainty estimates of the HAT and MSL cases are comparable, and hence the estimates were retained for both cases.

The aleatory uncertainty computations from the PRT_LE segment were adopted for the PRT_LW segment.

4.4.2 Scotian Slope Landslide Sources (TS1-TS8, TS6.5)

The source TS6.5 along the Scotian slope was analyzed for 3 scenarios with a range of volumes. The 3 scenarios are TS6.5_H0, TS6.5_M0 and TS6.5_L0, corresponding to landslide volumes of 165, 10, and 0.06 km^3, respectively. Linear regression was carried out with natural log of hazard parameter (wave runup or drawdown) as the dependent variable, and the natural log of landslide volume in km^3 as the independent variable. For all other sources (TS1–TS8), only one scenario was analyzed at the largest plausible scenario, corresponding to the landslide volume of 165 km^3. Using the slope (β) obtained from the TS6.5 slide's regression and the result of the single scenario for each of the other eight sources (TS1–TS8), we can compute corresponding intercepts for each source, thus obtaining a scaling relationship. Since one scenario per slide is computed, the uncertainty values computed for the TS6.5

slide are applied to the remaining eight sources for all cases.

As regards parametric aleatory uncertainty, since several parameters in the source model were at least partially correlated to landslide volume, an argument may be made to not include parametric aleatory uncertainty. Another approach is to calculate several scenarios where, at a constant volume, each parameter that may be a contributor is varied while holding others constant. Such calculations were made based on initial maximum tsunami amplitudes calculated by the landslide source model, which were assumed to be proportional to the response at the site for a given source location. Variation of slope in a plausible range produced the largest variations in maximum amplitude, at the constant largest plausible volume. We apply the slope variation as if it is independent of volume, although correlation exists in reality. We also apply variation at higher constant volume to all lower volumes. This is a conservative approach. We do not, however, consider the variation of other less varying parameters, which themselves are correlated with volume. The value computed for the HAT case was applied to the MSL case, and to the HAT and MSL cases for drawdown hazard.

4.4.3 Cumbre Vieja Volcano Landslides (CVV)

Although recurrence from three of the Canary Islands is considered, only the Cumbre Vieja volcano slides (CVV) on the La Palma Island were modelled using the hydrodynamic model—and were subsequently used for scaling relationships. The parametric aleatory uncertainty from the Scotian slope landslide TS6.5 was adopted for the CVV.

4.5. Results of the PTHA

Since our PTHA methodology closely follows the PSHA method, all the data products that are developed in PSHAs may be produced through our analysis. In general, as compared to PTHAs that only use scenarios consisting of large events, our use of scaling relationships, and the consequent inclusion of small events will generate slightly higher hazard estimates. As mentioned earlier, PTHA was computed at two stillwater tidal levels corresponding to
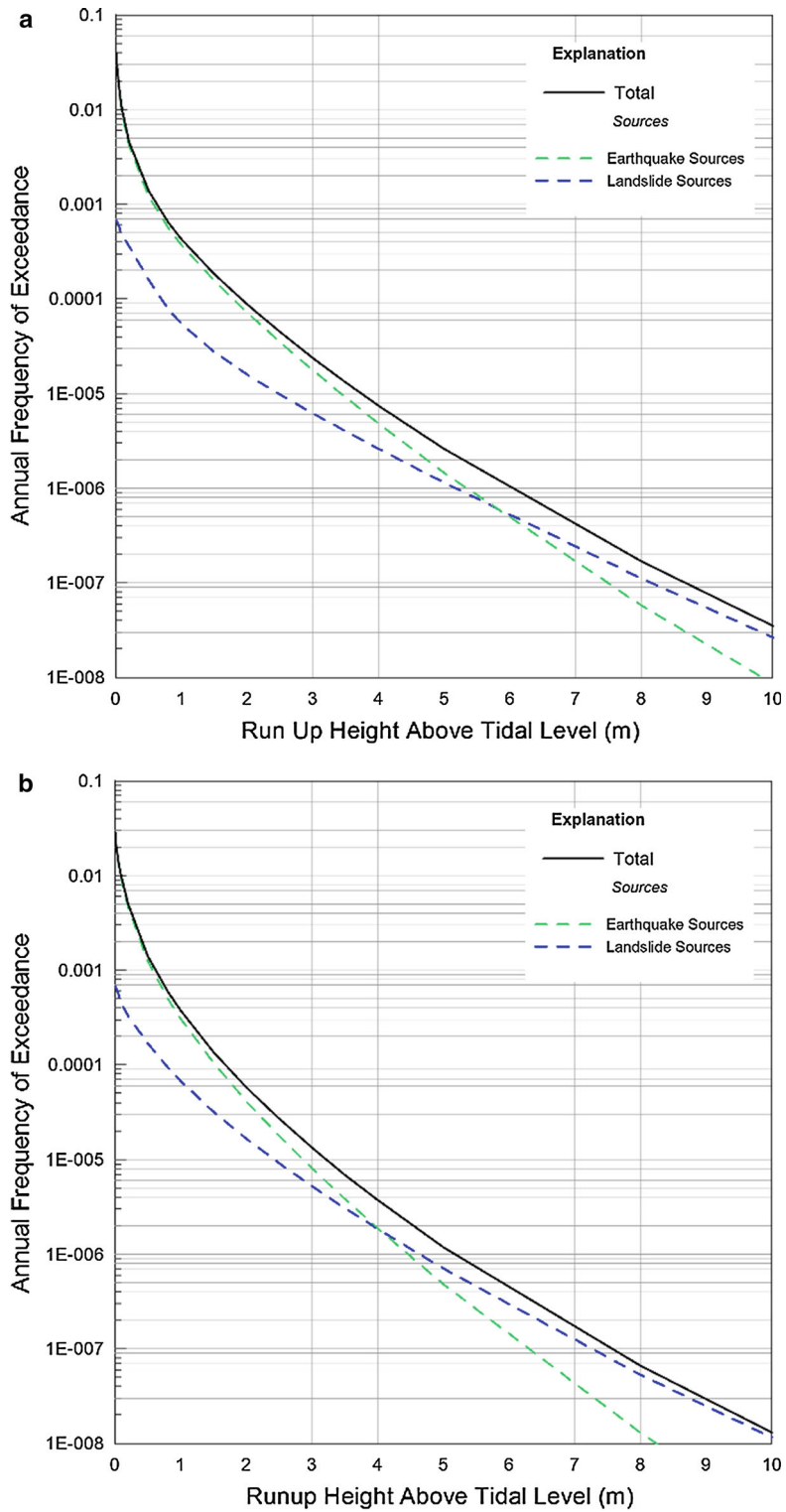
Figure 7
a Total tsunami hazard for wave runup at highest astronomical tide. **b** Total tsunami hazard for wave runup at mean sea level

HAT and MSL, and these hazard curves were then used along with computed probabilities of various tidal heights to generate the hazard curves that include tidal variation. We only present results and figures related to the wave runup hazard.

4.6. PTHA Hazard Results at Constant Tidal Levels

Figure 7 shows the mean hazard curves defining the mean frequency of exceeding specified wave runup levels over all of the sources of uncertainty. They show the mean total tsunami runup hazard for the highest astronomical tide (HAT) and mean sea level (MSL) cases, respectively, along with the contributions of the two source types (earthquake and landslide sources). Tsunami hazard at the site is dominated by earthquake sources, primarily the Puerto Rico subduction zone, at lower return periods (less than approximately 500,000 years). In particular, the runup tsunami hazard for the HAT case is dominated by earthquake sources at return periods less than approximately 1.43 million years (Fig. 7). For the MSL case, the earthquake sources are dominant at return periods less than about 500,000 years (Fig. 7). At greater return periods, the landslide sources are the dominant source type contributing to the tsunami hazard. Although the Canary Islands and Continental (Scotian) Slope landslide sources produce the highest runup at the site, earthquake sources dominate the hazard at the site because of the much shorter recurrence intervals for large earthquakes, on the order of hundreds to thousands of years, as compared to the greater than 100 kyr recurrence intervals for landslides (both on the continental slope and the Canary Islands).

The range in the total hazard results is shown in Fig. 8 by curves defining the mean, 5th, 16th, 50th (median), 84th, and 95th percentiles of the distributions for frequency of exceedance for runup at HAT and MSL computed from the logic tree. These fractile hazard curves define confidence intervals for the hazard resulting from uncertainties in specifying the inputs to the analysis. The results incorporate parametric epistemic uncertainties, but do not include epistemic uncertainty of using alternative models for tsunami prediction, as we chose the model providing generally higher results across a particular source type when both models were available. At a return period of 10,000 years, the 5th to 95th percentile spans about one-half of an order of magnitude (about half of a log cycle) for all cases. This uncertainty range is comparable to the PTHA study performed for the Diablo Canyon Power Plant (PGEC 2010), where the 50th to 90th fractile range at 10,000-year return period is about a quarter of a log cycle. The results show that the distribution for frequency of exceedance is skewed such that the mean hazard lies above the central point (median) of the distribution.

The runup tsunami hazard for the HAT case is higher than the MSL case, and the difference increases with increasing return period. Runup values at the 10,000-year return period (1.0E−4 annual frequency of exceedance) were calculated for all cases using interpolation between appropriate points on the hazard curve. The runup height corresponding to 10,000-year return period is 1.90 m for the HAT case, and 1.67 m for the MSL case.

4.7. Discussion of Contributions to Tsunami Hazard at Constant Tidal Levels

Figure 9 shows the total mean runup hazard at HAT and MSL for the earthquake sources, along with mean hazard for all individual earthquake sources. The Puerto Rico Trench (PRT) is the dominant earthquake source in all cases. The PRT produces higher runup at the site than the Azores-Gibraltar area sources for comparable size events (Table 4) because it is closer to the site, is oriented optimally to produce tsunamis directed at the site, and has fewer topographic barriers that would scatter the wave energy. Additionally, the PRT has similar or shorter recurrence intervals than other earthquake sources. At a return period of 10,000 years, the earthquake sources are the dominant source type contributing to the hazard, and the PRT is the dominant individual source contributor to the hazard.

Because PRT dominates the tsunami hazard at the site, we also show contributions from the components of the PRT rupture scenarios, together with the total PRT mean hazard (Fig. 10). The high magnitude PRT rupture scenario (PRTH) dominates the PRT mean hazard above 1.5 m for all cases. For low levels (less than about 1.5 m), the PRTH hazard flattens due to
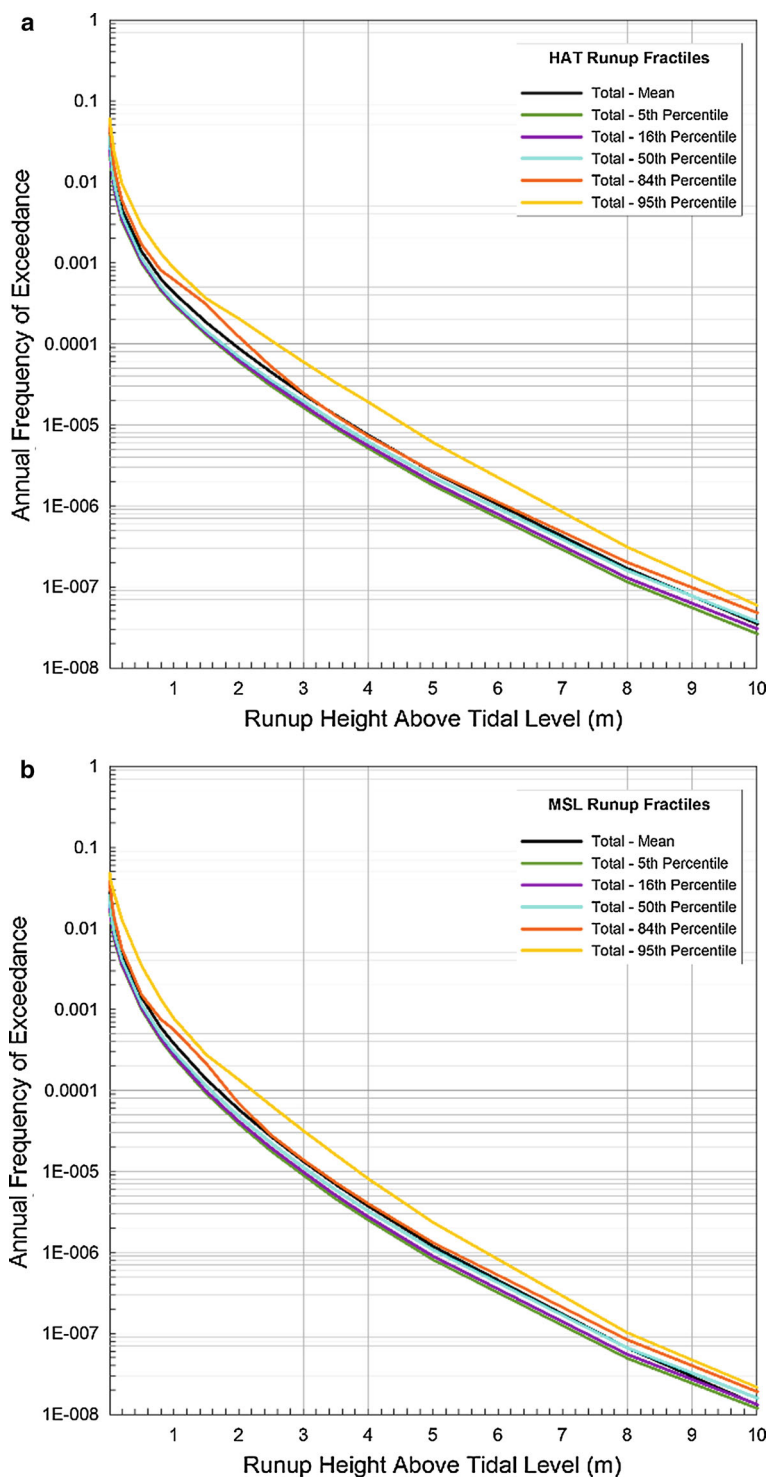
Figure 8
a Percentile hazard curves (aka Fractiles) for wave runup at highest astronomical tide. **b** Percentile hazard curves (aka Fractiles) for wave runup at mean sea level
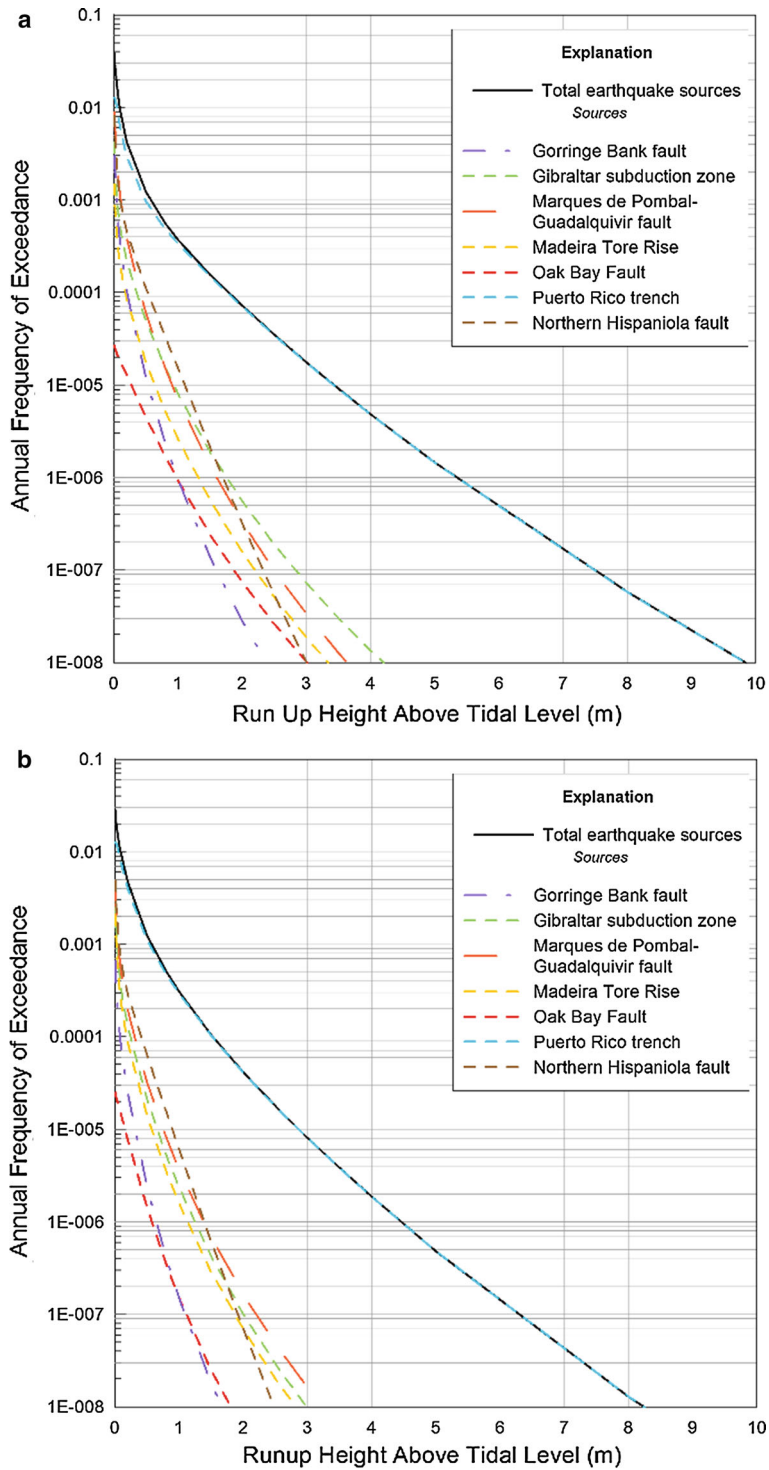
Figure 9
a Contribution of earthquake sources for wave runup at highest astronomical tide. **b** Contribution of earthquake sources for wave runup at mean sea level

lower recurrence rate of its event magnitude range, whereas the other segments (PRT_LW, PRT_LE) have higher hazard due to higher recurrence rates of their event magnitude ranges. For these low levels, the PRT_LW is the dominant contributor to the PRT mean hazard.

The four sources in the Azores–Gibraltar plate boundary area have a much lower contribution to the hazard than the PRT for all cases. Among the four sources, the Marques de Pombal fault (MPF) has the highest contribution to hazard for both cases, with the exception of HAT mean runup hazard where the GSZ produces higher hazard at return periods greater than 50,000 years (Fig. 9). The GSZ has a higher recurrence rate than the other three sources of the Azores–Gibraltar area (MPF, MTR, and GBF). The GSZ also has a higher maximum magnitude than other three sources. However, the runup produced by the GSZ for comparable magnitudes (<M 8.7) is lower than the other three sources. These effects compensate against each other, and the MPF, which has the second highest recurrence rate and a higher runup and drawdown than the GSZ, provides the highest relative contribution to the hazard among the four Azores–Gibraltar area sources.

Although the Oak Bay fault is located approximately 40 km from the site in the Bay of Fundy, it produces very little runup at the site (Table 4) because it is located primarily on land, is expected to produce strike-slip earthquakes (with minimal vertical displacement), the maximum magnitude of earthquakes it would produce is less than other sources, and has long recurrence intervals for large earthquakes (on the order of 50–100 kyr for M 6.5–7.0 earthquakes). As a result, the Oak Bay Fault is the one of the lowest contributors to the total mean hazard (Fig. 9).

Figure 11 shows the total mean runup hazard at HAT and MSL for the landslide sources along with mean hazard for the individual landslide source areas, and the individual sources for the Canary Islands source area. The contributions from the nine component sources of the Continental (Scotian) Slope, together with the total hazard of the Continental (Scotian) Slope are shown in Fig. 12, showing the runup hazard at HAT and MSL. For the runup landslide hazard, the Continental (Scotian) Slope

slides dominate the hazard except for low runup values (under about 1 m height), where the Canary Island sources are dominant contributors.

For the Canary Island sources, La Palma and Tenerife have identical contributions and the contribution from El Hierro is lower (Fig. 11). The same recurrence rate was calculated for La Palma and Tenerife; El Hierro has a lower calculated recurrence rate leading to the lower contribution to the hazard.

For the Continental (Scotian) Slope, TS6.5 has the largest contribution to the hazard for runup and location TS8 has the largest contribution to drawdown (Fig. 12). Other slide locations have higher and lower hazards based on their orientation and distance from the site. TS1 has the lowest contribution likely due to the distance from the site and being blocked by the Cape Cod peninsula and the shallow waters of the Georges Bank. A direct path from TS8 to the site is blocked by the Nova Scotia peninsula but it is one of the largest contributors likely due to the orientation and proximity to the site.

4.8. PTHA Hazard Results with Tidal Effects

Figure 13 shows the tsunami hazard including the effects of tidal variation for wave runup. As described in the PTHA methodology, the annual tidal variation dominates below +4.0 m for runup and above −4.0 m for drawdown. The combined hazard is presented in a range of 0–6 m for wave runup above +4 m MSL. Similarly, the combined hazard is presented in a range of 0 to −6 m for drawdown below −4 m MSL. Thus, for wave runup, the return period at +4 m MSL for hazard including tidal effects is about 14,500 years (mean annual exceedance frequency of 0.690E−04), and the return period at +5 m MLS for hazard including tidal effects is about 78,000 years.

4.9. Future Directions of Research

This study did not factor in climatic effects on landslide recurrence although there is some evidence that glacial cycles and changes in sea level may change continental slope landslide frequency. For the Atlantic Ocean (Lee 2009) the rate of landslide occurrence calculated during the last 5000 years of
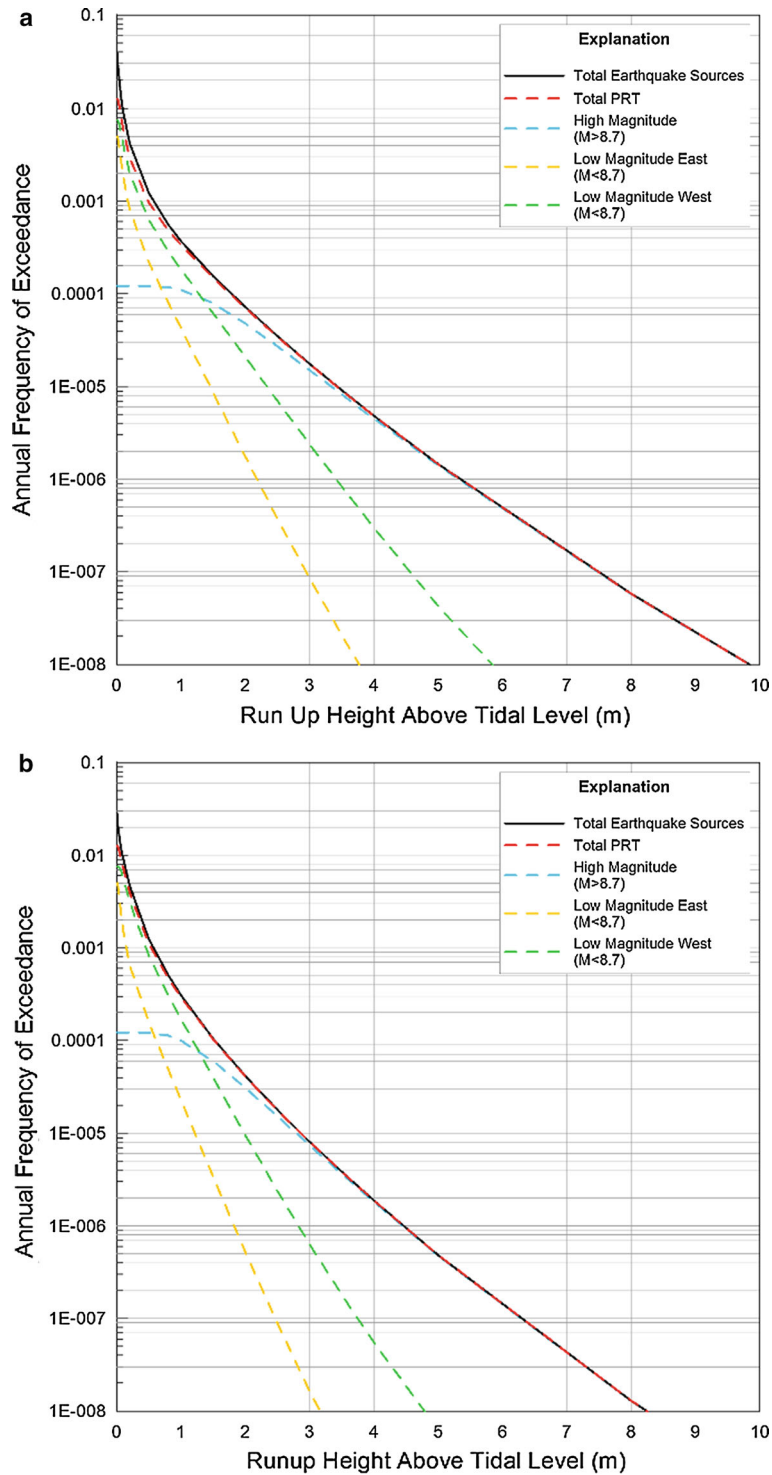
Figure 10
a Contribution of Puerto Rico Trench rupture scenarios for wave runup at highest astronomical tide. **b** Contribution of Puerto Rico Trench rupture scenarios for wave runup at mean sea level. The high magnitude PRT rupture scenario (PRTH) dominates the PRT mean hazard above 1.5 m for all cases
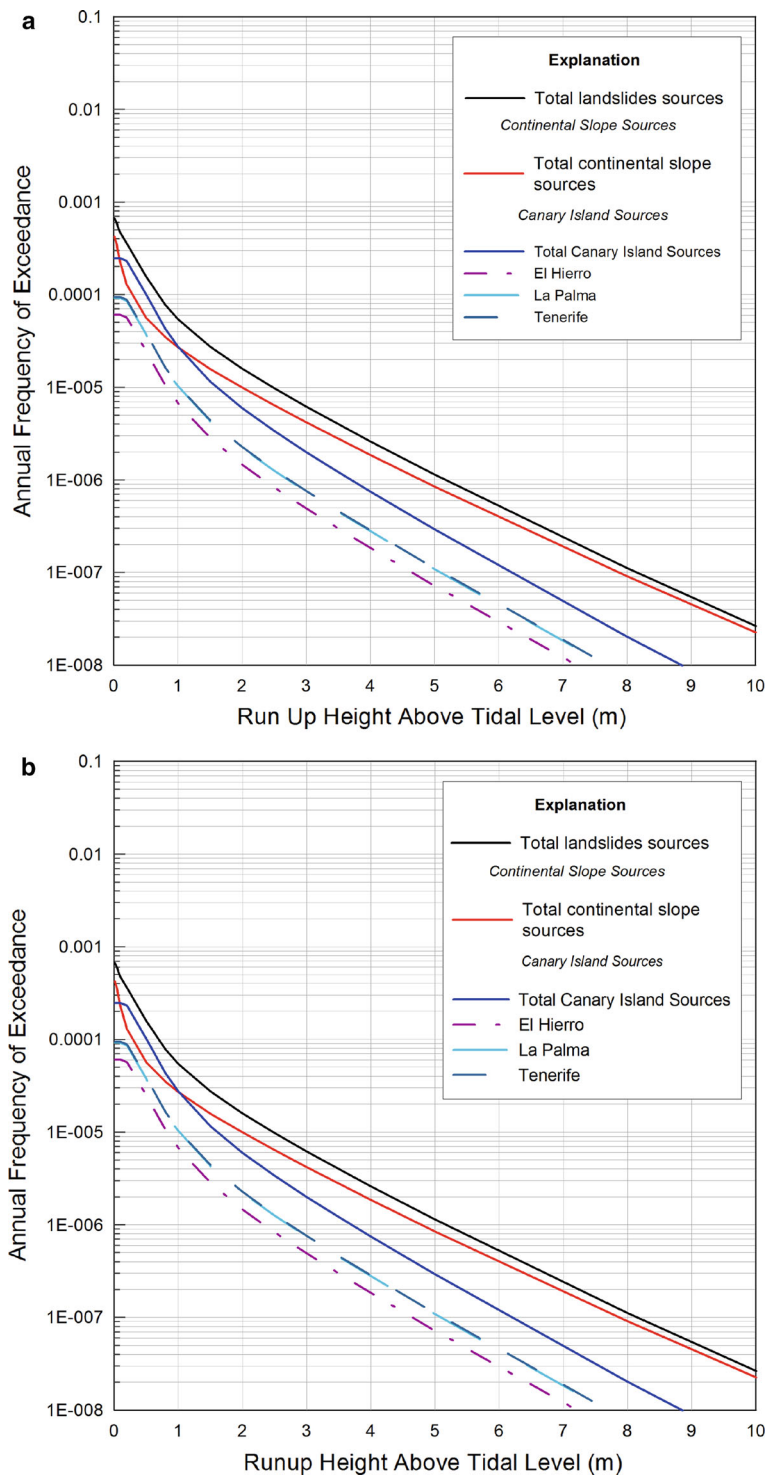
Figure 11

a Contribution of landslide sources for wave runup at highest astronomical tide. **b** Contribution of landslide sources for wave runup at mean sea level
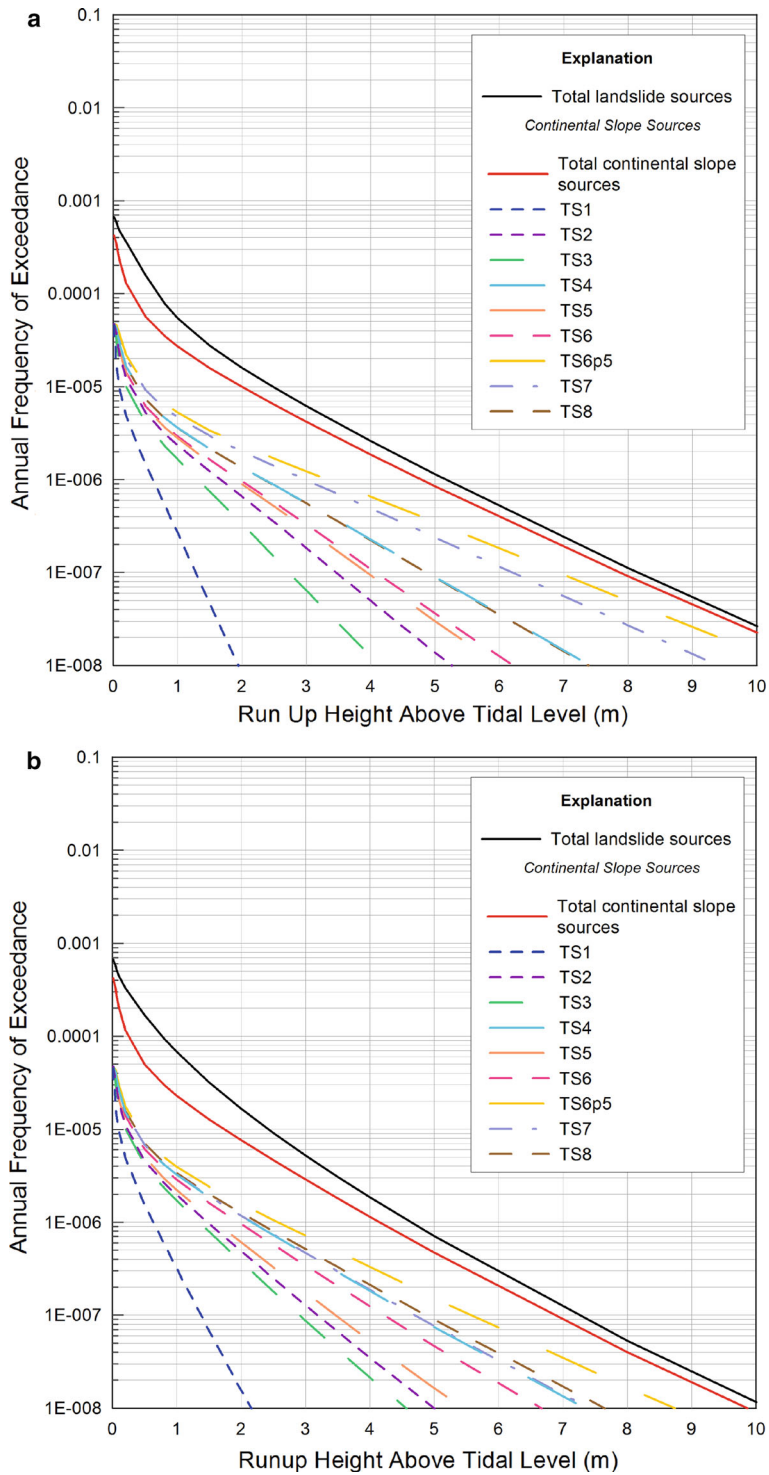
Figure 12
a Contribution of continental slope landslide sources for wave runup at highest astronomical tide. **b** Contribution of continental slope landslide sources for wave runup at mean sea level
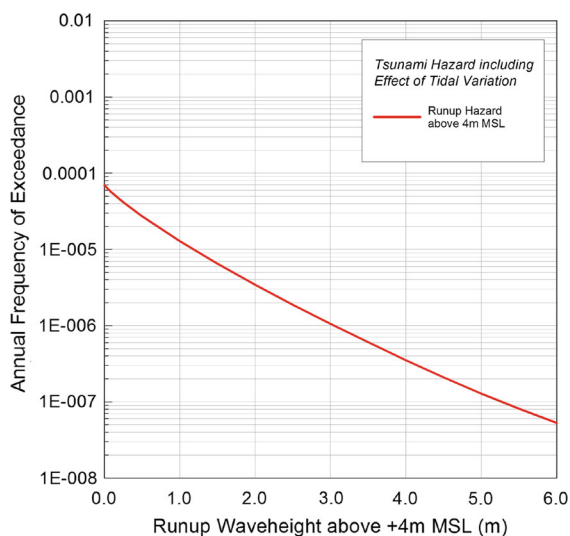
Figure 13
Tsunami hazard including effect of tidal variation for wave runup above +4 m MSL

interglacial time was 1.7–3.5 times lower than during the last glacial period, period and the deglacial period. Similarly, looking specifically at the margin of southeastern Canada, Piper et al. (2003) found a rate of 2 landslides per 10,000 years during the present interglacial and approximately 7 per 10,000 years during the last interglacial cycle. The relationship between glacial periods and landslide frequency on the Canary Islands may be different as Hunt et al. (2013) noted the largest events appear to occur during rising sea levels and highstands with only 10% of the landslides and turbidites occurring during glacial periods. Future studies may consider modifying the long-term rate of landslide occurrence to account for the predicted future climate and sea level.

Limitations in the probabilistic analysis performed in this study are generally related to development of scaling relationships between the initiating event size (earthquake magnitude or landslide volume) and wave runup, and the characterization of uncertainty. These issues can be alleviated to some extent by including more scenarios, or by combining analytical methods of computation with near-shore hydrodynamic modeling along with calibration as has been done in other recent studies. Because of the computational constraint on the number of individual scenarios, a multi-

stage approach is suggested, where first the highest plausible scenarios from each source are evaluated, then their relative contribution to the impact at site is considered, and only those with the higher impact or site inundating impact are further evaluated in detail. The epistemic uncertainty for this study did not include the uncertainty of using alternate models. Including this uncertainty would require computing additional scenarios using an alternate model. Depending on the threat faced by the site in question based upon the design return period (i.e., risk level), the analyst may decide to improve upon our methodologies to gain additional precision.

5. Conclusions

This study represents the first site-specific PTHA for a site in Eastern Canada, quantifying the aggregated site-specific tsunami hazard for the coastline near Point Lepreau, New Brunswick, based on the available knowledge of potential tsunamigenic source mechanisms in a wide range of source regions, from earthquake faults in the Bay of Fundy, regional submarine landslide sources, earthquake faults in the Puerto Rico trench and the Azores-Gibraltar region, and potential volcano flank collapses on the Canary Islands. This study demonstrates a new PTHA methodology that draws strongly from PSHA methods. It is also one of the few PTHA studies to include landslide, local fault and far-field subduction zone sources including the modeling of tsunami propagation and inundation at the site of interest. For locations where site-specific wave focusing, dispersion or resonance may be a factor simulating tsunami inundation is crucial for hazard analysis.

This study utilized a PTHA formulation that was analogous to the commonly applied PSHA methodology for assessing the hazard from rare events. Both earthquake and landslide sources were included in the analysis with recurrence relationships for a range of potential tsunami inducing events developed for each source. Further, both aleatory and epistemic uncertainties were included in the analysis. Scaling relationships were developed to relate the parameter denoting event size (e.g., earthquake magnitude or landslide volume) to the resulting tsunami wave

amplitude or runup. Further, both aleatory and epistemic uncertainties were included in the analysis. The study utilized hydrodynamic modeling of tsunami propagation and inundation, in both the nearshore and offshore regions to develop site-specific assessments of wave height and runup for a range of tsunami generation scenarios. Due to the extensive computation effort required, a limited number of scenarios were modeled for the various sources incorporated in the model. An initial set of modeling analyses were performed for scenarios representing central estimates of tsunami-generating events occurring on the various seismic sources. Then additional modeling was performed for alternative event sizes occurring on those sources that produced the largest effects at the site. Regression analyses were then used to develop site-specific scaling relationships for weight height and runup as a function of event site for the various tsunami-generating sources. The scaling relationships provided both median estimates of effects as well as aleatory variability in the amplitude of the tsunami effects.

The results of this study demonstrate that although PLGS is inland of a broad continental shelf and the site is protected from many open ocean sources by the Nova Scotia peninsula, tsunamis of more than a meter are possible in the Bay of Fundy. While even the most severe tsunami events considered in this study did not produce runup heights even close to inundating the ground level of the PLGS site, this study indicates that the tsunami hazard is nevertheless significant for many coastal communities in the region. Therefore, further research is warranted to quantify the site-specific hazard at the most vulnerable locations.

Similarly to other sites on the Atlantic Coast of North America, the greatest tsunami threat comes from Puerto Rico trench and the regional submarine landslide sources. The contribution of each of these sources will likely be refined in the future as further research refines estimates of their magnitude and frequency.

Acknowledgements

REFERENCES

Abadie, S. M., Harris, J. C., Grilli, S. T., & Fabre, R. (2012). Numerical modeling of tsunami waves generated by the flank collapse of the Cumbre Vieja Volcano (La Palma, Canary Islands), Tsunami source and near field effects. *Journal of Geophysical Research, 117*, C05030. doi:10.1029/2011JC007646.

Abrahamson, N. A., Somerville, P. G., & Cornell, C. A. (1990). Uncertainty in numerical strong ground motion predictions. In *Proceedings of the Fourth U.S. National Conference on Earthquake Engineering, Palm Springs, CA* (Vol. 1, pp. 407–416).

Amante, C., & Eakins, B. W. (2009). ETOPO1 1 Arc-Minute Global Relief Model, Procedures, Data Sources and Analysis. NOAA Technical Memorandum NESDIS NGDC-24. National Geophysical Data Center, NOAA. Accessed 2012.

Annaka, T., Satake, K., Sakakiyama, T., Yanagisawa, K., & Shuto, N. (2007). Logic-tree Approach for Probabilistic Tsunami Hazard Analysis and its Applications to the Japanese Coasts. *Pure and Applied Geophysics, 164*, 577–592.

Apotsos, A., Buckley, M., Gelfenbaum, G., Jaffe, B., & Vatvani, D. (2011). Nearshore Tsunami Inundation Model Validation: Toward Sediment Transport Applications. *Pure and Applied Geophysics, 168*(11):2097–2119

Atlantic and Gulf of Mexico Tsunami Hazard Assessment Group (AGMTHAG). (2008). "Evaluation of tsunami sources with the potential to impact the U.S. Atlantic and Gulf coasts", a report to the Nuclear Regulatory Commission, U.S. Geological Survey Administrative Report, p. 300.

Baptista, M. A., Miranda, J. M., & Luis, J. F. (2006). In search of the 31 March 1761 earthquake and tsunami source. *Bulletin of the Seismological Society of America, 96*, 713–721.

Barkan, R., ten Brink, U., & Lin, J. (2009). Far field tsunami simulations of the 1755 Lisbon earthquake, implications for tsunami hazard to the U.S. east coast and the Caribbean. *Marine Geology, 264*, 109–122.

Booth, J. S., O'Leary, D. W., Popenoe, P., & Danforth, W. W. (1993). U.S. Atlantic slope landslides, their distribution, general attributes, and implications. In W.C. Schwab, H.J. Lee & D.C. Twichell (Eds.), *Submarine landslides, selected studies in the U.S. Exclusive Economic Zone* (pp. 14–22) USGS Bulletin 2002.

British Oceanographic Data Centre (BODC). (2014). General Bathymetric Chart of the Oceans (GEBCO_08), http://www.gebco.net/about_us/news_and_events/gebco_08_release.html. Accessed 11 June 2014.

Buforn, E., Udias, A., & Mezcua, J. (1988). Seismicity and focal mechanism in south Spain. *Bulletin of the Seismological Society of America, 88*, 2008–2224.

Burke, K.B.S. & Stringer, P. (1993). A search for neotectonic features in the Passamaquoddy Bay region, southwestern New Brunswick. Current Research, Part D, Eastern Canada and National and General Programs, Geological Survey of Canada, Paper 93-1D, pp. 93–102

Reprinted from the journal

Calais, E., DeMets, C., & Nocquet, J. M. (2003). Evidence for a post-3.16-Ma change in Nubia-Eurasia-North America plate motions? *Earth and Planetary Science Letters, 6825*, 1–12.

Calais, E., Mazabraud, Y., Mercier de Lepinay, B., Mann, P., Mattioli, G., & Jansma, P. (2002). Strain partitioning and fault slip rates in the northeastern Caribbean from GPS measurements. *Geophysical Research Letters, 29*, 3-1–3-4.

Chaytor, J., ten Brink, U. S., Solow, A. R., & Andrews, B. D. (2009). Size distribution of submarine landslides along the U.S. Atlantic Margin. *Marine Geology, 264*, 16–27.

Chaytor, J. D., Twichell, D., & ten Brink, U. S. (2012). Reevaluation of the Munson–Nygren–Retriever submarine landslide complex, Georges Bank Lower Slope, Western North Atlantic. In Y. Yamada, K. Kawamura, K. Ikehara, Y. Ogawa, R. Urgeles, D. Mosher, J. Chaytor, M. Strasser (Eds.), *Submarine Mass Movements and their Consequences, Advances in Natural and Technological Hazards Research* (Vol. 31, pp. 131–145).

Chen, Q. (2006). Fully nonlinear Boussinesq-type equations for waves and currents over porous beds. *Journal of Engineering Mechanics, 132*, 220–230.

Cornell, C.A. (1968). Engineering seismic risk analysis. *Bulletin of the Seismological Society of America, 58(5)*, 1583–1606.

Cornell, C. A. (1971). Probabilistic analysis of damage to structures under seismic loads. In *Dynamic Waves in Civil Engineering*. London: Wiley.

Day, S. J., Watts, P., Grilli, S. T., & Kirby, J. T. (2005). Mechanical models of the 1975 Kalapana, Hawaii earthquake and tsunami. *Marine Geology, 215*, 59–92.

DeMets, C., Gordon, R. G., & Argus, D. F. (2010). Geologically current plate motions. *Geophysical Journal International, 181*, 1–80.

DeMets, C., Gordon, R., Argus, D., & Stein, S. (1990). Current plate motions. *Geophysical Journal International, 101*, 425–478.

Dolan, J.F., & Wald, D. (1998). The 1943-1953 north-central Caribbean earthquakes: active tectonic setting, seismic hazards, and implications for Caribbean-North America plate motions. In Dolan, J. & Mann, P. (Eds.), *Active strike-slip and collisional tectonics of the Northern Caribbean Plate Boundary Zone*. Geological Society of America Special Paper 326, Boulder, Colorado, pp. 143–169.

Electric Power Research Institute (EPRI), U.S. Department of Energy, and U.S. Nuclear Regulatory Commission. (2012). Technical Report, Central and Eastern United States Seismic Source Characterization for Nuclear Facilities.

Enet, F., & Grilli, S. T. (2005). Tsunami Landslide Generation: Modelling and Experiments. In *Proc. 5th Intl. on Ocean Wave Measurement and Analysis*, IAHR Publication, p. 10.

Enet, F., & Grilli, S. T. (2007). Experimental study of tsunami generation by three-dimensional rigid underwater landslides. *Journal of Waterway, Port, Coastal, and Ocean Engineering, 133*, 442–454.

Enet, F, Grilli, S. T., & Watts, P. (2003), Laboratory experiments for tsunamis generated by underwater landslides: comparison with numerical modeling. In *Proc. 13th Offshore and Polar Engineering Conference* (pp. 372–379).

Fine, I. V., Rabinovich, A. B., Bornhold, B. D., Thomson, R. E., & Kulikov, E. A. (2005). The Grand Banks landslide-generated tsunami of November 18, 1929, preliminary analysis and numerical modeling. *Marine Geology*, 45–57.

Fukao, Y. (1973). Thrust faulting at a lithospheric plate boundary, the Portugal earthquake of 1969. *Earth and Planetary Science Letters, 18*, 205–216.

Gates, O. (1989). The geology and geophysics of the Passamaquoddy Bay area, Maine and New Brunswick, and their bearing on local subsidence. In W. A. Anderson & H. W. Borns (Eds.), *Neotectonics of Maine* (Vol. 40, pp. 11–24), Maine Geological Survey.

Geist, E. L., Lynett, P. J., & Chaytor, J. D. (2009). Hydrodynamic modeling of tsunamis from the Currituck landslide. *Marine Geology, 264*, 41–52.

Geist, E. L., & Parsons, T. (2009). Assessment of source probabilities for potential tsunamis affecting the U.S. Atlantic coast. *Marine Geology, 264*, 98–108. doi:10.1016/j.margeo.2008.08.005.

Gica, E., Spillane, M., Titove, V. V., Chamberline, C.D., & Newman, J.C. (2008). *Development of the Forecast Propagation Database for Noaa's Short-Term Inundation Forecast for Tsunamis (SIFT)*, NOAA Technical Memorandum OAR PMEL-139, p. 89.

Giles, M. K., Mosher, D. C., Piper, D. J. W., & Wach, G. D. (2010). Mass transport deposits on the southwestern newfoundland slope, submarine mass movements and their consequences. In D.C. Mosher, R.C. Shipp, L. Moscardelli, J.D. Chaytor, C.D.P. Baxter, H.J. Lee, R. Urgeles (Eds.), *Advances in Natural and Technological Hazards Research* (Vol. 28, pp. 657–665).

González, F. I., Geist, E. L., Jaffe, B., Kânoğlu, U., Mofjeld, H., Synolakis, C. E., Titov, V. V., Arcas D., Bellomo, D., Carlton, D., Horning, T., Johnson, J., Newman, J., Parsons, T., Peters, R., Peterson, C., Priest, G., Venturato, A., Weber, J., Wong, F., & Yalciner, A. (2009) Probabilistic tsunami hazard assessment at Seaside, Oregon, for near- and far-field seismic sources. *Journal of Geophysical Research, 114*(C11), 1978–2012. doi:10.1029/2008JC005132.

Gràcia, E., Vizcaino, A., Escutia, C., Asioli, A., Rodés, A., Garcia-Orellano, J., et al. (2010). Holocene earthquake record offshore Portugal (SW Iberia), testing turbidite paleoseismology in a slow-convergence margin. *Quaternary Science Reviews, 29*, 1156–1172.

Grilli, S. T. (1997). Fully nonlinear potential flow models used for long wave runup prediction. In H. Yeh, P. Liu, & C. Synolakis (Eds.), *Long-Wave Runup Models* (pp. 116–180). Singapore: World Scientific Publishing.

Grilli, S. T., Dubosq, S., Pophet, N., Pérignon, Y., Kirby, J. T., & Shi, F. (2010). Numerical simulation and first-order hazard analysis of large co-seismic tsunamis generated in the Puerto Rico trench: near-field impact on the North shore of Puerto Rico and far-field impact on the US East Coast. *Natural Hazards Earth Systems Science., 10*, 2109–2125.

Grilli, A.R., & Grilli, S. T. (2013a). *Modeling of Tsunami Generation, propagation and regional impact along the upper U.S. east coast from the Azores Convergence Zone*. Draft report to NTHMP, p. 13.

Grilli, A. R., & Grilli, S. T. (2013b). *Far-field tsunami impact on the US East Coast from an extreme flank collapse of the Cumbre Vieja volcano (Canary Islands)*. Draft report to NTHMP, p. 13.

Grilli, S. T., Harris, J.C., & Bakhsh, T. T. (2011). *Literature review of tsunami sources affecting tsunami hazard along the US East Coast*. Research Report No. CACR-11-08, p. 60.

Grilli, S.T., O'Reilly, C., & Bakhsh, T. T. (2013). *Modeling of SMF tsunami generation and regional impact along the upper U.S. East Coast.* Research Report No. CACR-13-05, p. 46.

Grilli, S. T., O'Reilly, C., Harris, J. C., Bakhsh, T. T., Tehranirad, B., Banihashemi, S., et al. (2015). Modeling of SMF tsunami hazard along the upper US East Coast: detailed impact around Ocean City, MD. *Natural Hazards*. doi:10.1007/s11069-014-1522-8.

Grilli, S. T., Taylor, O. S., Baxter, C. D. P., & Maretzki, S. (2009). A probabilistic approach for determining submarine landslide tsunami hazard along the upper east coast of the United States. *Marine Geology, 264*, 74–97.

Grilli, S. T., Vogelmann, S., & Watts, P. (2002). Development of a 3D numerical wave tank for modeling tsunami generation by underwater landslides. *Engineering Analysis with Boundary Elements, 264*, 301–313.

Grilli, S. T., & Watts, P. (1999). Modeling of waves generated by a moving submerged body, Applications to underwater landslides. *Engineering Analysis with Boundary Elements, 23*, 645–656.

Grilli, S. T., & Watts, P. (2005). Tsunami generation by submarine mass failure part I, modeling, experimental validation, and sensitivity analysis. *Journal of Waterway, Port, Coastal, and Ocean Engineering, 131*, 283–297.

Grilli, S. T, Ioualalen, M., Asavanant, J., Shi, F., Kirby, J. T., & Watts, P. (2007) Source Constraints and Model Simulation of the December 26, 2004, Indian Ocean Tsunami. *Journal of Waterway, Port, Coastal, and Ocean Engineering, 133(6)*, 414–428

Grimison, N. L., & Chen, W. (1986). The Azores-Gibraltar plate boundary, focal mechanisms, depth of earthquakes and their tectonic implications. *Journal of Geophysical Research, 91*, 2029–2047.

Gutscher, M.-A., Baptista, M. A., & Miranda, J. M. (2006). The Gibraltar Arc seismogenic zone (part 2), constraints on a shallow east dipping fault plane source for the 1755 Lisbon earthquake provided by tsunami modeling and seismic intensity, *Tectonophysics, 426*, 153–166, doi:10.1016/j.tecto.2006.02.025.

Harris, J. C., Grilli, S. T., Abadie, S., & Bakhsh, T. T. (2012). Near- and far-field tsunami hazard from the potential flank collapse of the Cumbre Vieja Volcano. In *Proceedings of the twenty-second International Offshore and Polar Engineering Conference* (p. 242).

Hayward, N., Watts, A. B., Westbrook, G. K., & Collier, J. S. (1999). A seismic reflection and GLORIA study of compressional deformation in the Gorringe Bank region, eastern North Atlantic. *Geophysical Journal International., 138*, 831–850.

Horillo, J., Grilli, S. T., Nicolsky, D., Roeber, V., & Zhang, J. (2014). Performance benchmarking tsunami models for NTHMP's inundation mapping activities. Pure and Applied Geophysics. doi:10.1007/s00024014-0891.

Hunt, J. E. (2012). *Determining the provenance, recurrence, magnitudes and failure mechanisms of submarine landslides from the Moroccan Margin and Canary Islands using distal turbidite records.* Dissertation, University of South Hampton. p. 374.

Hunt, J. E., Talling, P. J., Clare, M. A., Jarvis, I., & Wynn, R. B. (2014). Long-term (17 Ma) turbidite record of the timing and frequency of large flank collapses of the Canary Islands. *Geochemistry, Geophysics, Geosystems, 15*, 3322–3345.

Hunt, J. E., Wynn, R.B., Talling, P. J., & Masson, D. G. (2013). Multistage collapse of eight Western Canary Island landslides in the last 1.5 Ma, sedimentological and geochemical evidence from subunits in submarine flow deposits. *Geochemistry, Geophysics, Geosystems, 14*, 2159–2181. doi:10.1002/ggge.20138.

Huppertz, T. J., Piper, D. J. W., Mosher, D. C., & Jenner, K. (2010). The significance of mass-transport deposits for the evolution of a proglacial continental slope. In Mosher, D. C., Shipp, R. C., Moscardelli, L., Chaytor, J. D., Baxter, C. D. P., Lee, H. J., & Urgeles, R. (Eds.), *Submarine mass movements and their consequences. Advances in natural and technological hazards research* (Vol. 28, pp. 631–641). Netherlands: Springer.

Ioualalen, M., Asavanant, J., Kaewbanjak, N., Grilli, S. T., Kirby, J.T., & Watts, P. (2007). Modeling the 26 December 2004 Indian Ocean tsunami, case study of impact in Thailand. *Journal of Geophysical Research, 112*, C07024. doi:10.1029/2006JC03850.

Jansma, P., Mattioli, G. S., Lopez, A., DeMets, C., Dixon, T. H., Mann, P., et al. (2000). Neotectonics of Puerto Rico and the Virgin Islands, northeastern Caribbean, from GPS Geodesy. *Tectonics., 19*, 1021–1037.

Johnston, A. C. (1996). Seismic movement assessment of earthquakes in stable continental regions; III, New Madrid 1811-1812, Charleston 1886 and Lisbon 1755. *Geophysical Journal International, 126*, 314–344.

Kirby, J. T., Shi, F., Tehranirad, B., Harris, J. C., & Grilli, S. T. (2013). Dispersive tsunami waves in the ocean: Model equations and sensitivity to dispersion and Coriolis effects. *Ocean Modeling, 62*, 39–55.

Krentz, S. (2009). *Potentially tsunamigenic layer in late Holocene Great South Bay, Long Island, New York, constraints on origins, processes, and effects.* Master's Thesis, Vanderbilt University, p. 77.

Kulkarni, R. B., Youngs, R. R., & Coppersmith, K. J. (1984). Assessment of confidence intervals for results of seismic hazard analysis. In *Proceedings of the Eighth World Conference on Earthquake Engineering*, San Francisco, California (Vol. 1, pp. 263–270).

LaForge, R. C., & McCann, W. R. (2005). A seismic source model for Puerto Rico, for use in probabilistic ground motion hazard analyses. In P. Mann (Ed.), *Active tectonics and seismic hazards of Puerto Rico, the Virgin Islands, and offshore areas* (pp. 223–248). Geological Society of America Special Paper 385.

Lee, H. J. (2009). Timing of occurrence of large submarine landslides on the Atlantic Ocean margin. *Marine Geology, 264*, 53–64.

Leonard, L. J., Rogers, G. C., & Mazzotti, S. (2012). *A preliminary tsunami hazard assessment of the Canadian coastline.* Geological Survey of Canada, Open File 7201, p. 126.

Locat, J., Lee, H., ten Brink, U., Twichell, D. C., Geist, E. L., & Sansoucy, M. (2009). Geomorphology, stability and mobility of the Currituck slide. *Marine Geology., 264*, 28–40.

Locat, J., ten Brink, U. S., & Chaytor, J. D. (2013). A geomorphological analysis of the Veatch slide complex off Massachusetts, U.S.A. In S. Krastel, J.-H. Behrmann, D. Völker, M. Stipp, C. Berndt, R. Urgeles, J. Chaytor, K. Huhn, M. Strasser, & C.B. Harbitz (Eds.), *Submarine Mass Movements and Their Consequences, Advances in Natural and Technological Hazards Research* (Vol. 37, pp. 371–380).

Løvholt, F., Pedersen, G., & Gisler, G. (2008). Oceanic propagation of a potential tsunami from the La Palma Island. *Journal of Geophysical Research, 113*, C09026. doi:10.1029/2007JC004603.

Luque, L., Lario, J., Civis, J., Silva, P. G., Zazo, C., Goy, J. L., et al. (2002). Sedimentary record of a tsunami during Roman

times, Bay of Cadiz, Spain. *Journal of Quaternary Science, 17*, 623–631.

Mader, C. L. (2001). Modeling the La Palma landslide tsunami. *Science of Tsunami Hazards, 19*, 150–170.

Maretzki, S., Grilli, S., & Baxter, C. D. P. (2007). Probabilistic SMF tsunami hazard assessment for the upper East Coast of the United States. In V. Lykousis, D. Sakellariou, & J. Locat (Eds.), *Submarine Mass Movements and Their Consequences, Advances in Natural and Technological Hazards Research* (Vol. 27, pp. 377–385).

Masson, D. G., Watts, A. B., Gee, M. J. R., Urgeles, R., Mitchell, N. C., Le Bas, T. P., et al. (2002). Slope failures on the flanks of the western Canary Islands. *Earth Science Reviews, 57*, 1–35.

Matthews, M., Ellsworth, W., & Reasenberg, P. (2002). A Brownian model for recurrent earthquakes. *Bulletin of the Seismological Society of America., 92*, 2233–2250.

McAdoo, B. G., Pratson, L. F., & Orange, D. L. (2000). Submarine landslide geomorphology, US continental slope. *Marine Geology, 169*, 103–136.

McCann, W. R. (1985). On the earthquake hazard of Puerto Rico and the Virgin Islands. *Bulletin of the Seismological Society of America, 75*, 251–262.

McGuire, R. K. (2004). Seismic hazard and risk analysis, Earthquake Engineering Research Institute, Second Monograph Series, MNO-10, p. 239.

Moore, A. L., McAdoo, B. G., & Ruffman, A. (2007). Landward fining from multiple sources in a sand sheet deposited by the 1929 Grand Banks tsunami, Newfoundland. *Sedimentary Geology, 200*, 336–346.

Morales, J. A., Borrego, J., San Miguel, E. G., López-González, N., & Carro, B. (2008). Sedimentary record of recent tsunamis in the Huelva Estuary (southwestern Spain). *Quaternary Science Reviews, 27*, 734–746.

Mosher, D. C., & Campbell, D. C. (2011). The Barrington Submarine Mass-Transport Deposit, Western Scotian Slope, Canada. Mass-Transport Deposits in Deepwater Settings, Society of Economic Paleontologists and Mineralogists, Special Publications 96, pp. 151–159.

Mosher, D. C., & Piper, D. J. W. (2007). Analysis of multibeam seafloor imagery of the Laurentian Fan and the 1929 Grand Banks landslide area. In V. Lykousis, D. Sakellariou, & J. Locat (Eds.), *Submarine Mass Movements and Their Consequences, Advances in Natural and Technological Hazards Research* (pp. 77–88).

Mosher, D. C., & Piper, D. J. W. (2007). Analysis of multibeam seafloor imagery of the Laurentian Fan and the 1929 Grand Banks landslide area. In V. Lykousis, D. Sakellariou, & J. Locat (Eds.), *Submarine Mass Movements and Their Consequences* (pp. 77–88).

Mueller, C. S., Frankel, A. D., Petersen, M. D., & Leyendecker, E. V. (2003). *Documentation for the 2003 USGS Seismic Hazard Maps for Puerto Rico and the U.S. Virgin Islands*. USGS Open File Report 03-379, p. 12.

Muir-Wood, R., & Mignan, A. (2009). A phenomenological reconstruction of the Mw 9 November 1st 1755 earthquake source. In L.A. Mendes-Victor, C.S. Olivera, J. Azevedo, & A. Ribeiro (Eds.) *The 1755 Lisbon earthquake*, revisited, Geotechnical, Geological, and Earthquake Engineering (Vol. 7, pp. 121–146).

National Center for Environmental Information (NCEI). (2014). National Geophysical Data Center, www.ngdc.noaa.gov Accessed 13 Oct 2014.

Okada, Y. (1985). Surface deformation due to shear and tensile faults in a half-space. *Bulletin of the Seismological Society of America, 75*, 1135–1154.

Pacific Gas & Electric Company (PGEC). (2010). *Methodology for Probabilistic Tsunami Hazard Analysis, Trial Application for the Diablo Canyon Power Plant Site*. Submitted to the PEER Workshop on Tsunami Hazard Analyses for Engineering Design Parameters, Berkeley, CA, p. 197.

Pararas-Carayannis, G. (2002). Evaluation of the threat of mega tsunami generation from postulated massive slope failures of island stratovolcanoes on La Palma, Canary Islands, and on the island of Hawaii. *Science of Tsunami Hazards, 20*, 251–277.

Piper, D.J.W., Mosher, D.C., Gaulry, B.-J., Jenner, K., & Campbell, D.C. (2003). The Chronology and Recurrence of Submarine Mass Movements on the Continental Slope off Southeastern Canada. Locat, J. and Mienert, J. (editors), Submarine Mass Movements and Their Consequences, pp. 299–306

Piper, D. J. W., Mosher, D. C., & Campbell, D. C. (2012). Controls on the distribution of major types of submarine landslides. In J. J. Clague & D. Stead (Eds.), *Landslides, Types, Mechanisms and Modeling* (pp. 95–107). Cambridge University Press.

Rikitake, T., & Aida, I. (1988). Tsunami Hazard probability in Japan. *Bulletin of the Seismological Society of America., 78*, 1268–1278.

Roworth, E., & Signell, R. (1999). *Construction of digital bathymetry for the Gulf of Maine*. USGS Open File Report, 98-801.

Ruffman, A. (1997). Tsunami runup mapping as an emergency preparedness planning tool: the 1929 tsunami in St. Lawrence, Newfoundland, Geomarine Associates. Contract Report for Emergency Preparedness Canada, Ottawa, Ontario (Vol. 1, p. 107).

Ruffman, A. (2006). Documentation of the farfield parameters of the November 1, 1755 "Lisbon" tsunami along the shores of the western Atlantic Ocean, Program and Abstracts, International Tsunami Society Third Tsunami Symposium.

Scheffers, A., & Kelletat, D. (2005). Tsunami relics on the coastal landscape west of Lisbon, Portugal. *Science of Tsunami Hazards, 23*, 3–16.

Service New Brunswick. (2014). GeoNB DEM Data Catalogue, http://www.snb.ca/geonb1/e/DC/catalogue-E.asp.

Shi, F., Kirby, J. T., Harris, J. C., Geiman, J. D., & Grilli, S. T. (2012a). A high-order adaptivetime-stepping TVD solver for Boussinesq modeling of breaking waves and coastal inundation. *Ocean Modelling, 43–44*, 36–51.

Shi, F., Kirby, J. T., & Tehranirad, B. (2012b). *Tsunami benchmark results for spherical coordinate*. Center for Applied Coastal Research Report, CACR 2012-02, University of Delaware, Newark, Delaware.

Stelling, G. S., & Duinmeijer, S. P. A. (2003). A staggered conservative scheme for every Froude number in rapidly varied shallow water flows. *International Journal Numerical Methods in Fluids, 43*, 1329–1354.

Stelling, G. S. & Leendertse, J. J. (1992). Approximation of convective processes by cyclic AOI methods. In M. L. Spaulding, K. Bedford, & A. Blumberg (Eds.) *Estuarine and coastal modeling, Proceedings 2nd Conference on Estuarine and Coastal Modelling* (pp. 771–782). Tampa: ASCE.

Sykes, L., McCann, W., & Kafka, A. (1982). Motion of Caribbean plate during last seven million years and implications for earlier Cenozoic movements. *Journal of Geophysical Research, 87*, 10656–10676.

Tappin, D. R., Watts, P., & Grilli, S. T. (2008). The Papua New Guinea tsunami of 1998, anatomy of a catastrophic event. *Natural Hazards and Earth System Sciences., 8*, 243–266.

Tehranirad, B., Harris, J. C., Grilli, A. R., Grilli, S. T., Abadie, S., Kirby, J. T., et al. (2015). Far-field tsunami hazard on the western European and US east coast from a large scale flank collapse of the Cumbre Vieja volcano, La Palma. *Pure and Applied Geophysics, 172*, 3589–3616.

Tehranirad, B., Shi, F., & Kirby, J. T. (2012). Tsunami benchmark results for spherical coordinate, Center for Applied Coastal Research Report, CACR 2013-10, University of Delaware, Newark, Delaware.

Tehranirad, B., Shi, F., Kirby, J. T., Harris, J. C., & Grilli, S. (2013). Tsunami benchmark results for fully nonlinear Boussinesq wave model FUNWAVE-TVD, Version 2.1. Research Report No. CACR-13-10, Center for Applied Coastal Research, University of Delaware.

ten Brink, U. S., Chaytor, J. D., Geist, E. L., Brothers, D. S., & Andrews, B. D. (2014). Assessment of tsunami hazard to the U.S. Atlantic margin. *Marine Geology, 353*, 31–54.

ten Brink, U. S., Lee, H. J., Geist, E. L., & Twichell, D. (2009). Assessment of tsunami hazard to the US East Coast using relationships between submarine landslides and earthquakes. *Marine Geology, 264*, 65–73.

Thiebot, E., & Gutscher, M.-A. (2006). The Gibraltar Arc seismogenic zone (part 1), constraints on a shallow east dipping fault plane source for the 1755 Lisbon earthquake provided by seismic data, gravity and thermal modeling. *Tectonophysics., 426*, 135–152.

Thio, H. K., Somerville, P., & Polet, J. (2010). Probabilistic Tsunami Hazard in California, Pacific Earthquake Engineering Research Center (PEER), College of Engineering, University of California, Berkeley, PEER Report 2010/108.

Thomson, R. E., Rabinovich, A. B., & Krassovski, M. V. (2007). Double jeopardy, Concurrent arrival of the 2004 Sumatra tsunami and storm-generated waves on the Atlantic coast of the United States and Canada. *Geophysical Research Letters, 34*, L15607. doi:10.1029/2007GL030685.

Tuttle, M. P., Mahani, A. B., Dyer-Williams, K., MacKay, A. S., & Busch, T. A. (2014). Paleoseismology project in the region of the Lepreau Nuclear Generating Station, prepared for the New Brunswick Power Nuclear Corporation, p. 290.

Tuttle, M. P., Ruffman, A., Anderson, T., & Jeter, H. (2004). Distinguishing tsunami deposits from storm deposits along the coast of northeastern North America: Lessons learned from the 1929 Grand Banks tsunami and the 1991 Halloween storm. *Seismological Research Letters, 75*, 117–131.

Vatvani, D. (2005). Hindcast of tsunami flooding in Aceh-Sumatra. In *Proceedings of the Fifth International Symposium on Ocean Wave Measurement and Analysis-Waves*.

Van Veen B.A.D, Vatvani D., Zijl F., (2014) Tsunami flood modelling for Aceh & west Sumatra and its application for an early warning system. *Continental Shelf Research, 79*, 46–53

Ward, S. N., & Day, S. (2001). Cumbre Vieja Volcano—potential collapse and tsunami at La Palma, Canary Islands. *Geophysical Research Letters, 28*, 3397–3400.

Watts, P., & Grilli, S. T. (2003). Underwater landslide shape, motion, deformation, and tsunami generation. In *Proc., 13th Offshore and Polar Engineering Conf., International Society of Offshore and Polar Engineers*, Cupertino, CA (Vol. 3, pp. 364–371).

Watts, P., Grilli, S. T., Kirby, J. T., Fryer, G. J., & Tappin, D. R. (2003). Landslide tsunami case studies using Boussinesq model and a fully nonlinear tsunami generation model. *Natural Hazards and Earth Systems Science, 3*, 391–402.

Watts, P., Grilli, S., Tappin, D., & Fryer, G. (2005). Tsunami generation by submarine mass failure, II, predictive equations and case studies. *Journal of Waterway, Port, Coastal, and Ocean Engineering, 131*, 298–310.

Wynn, R. B., & Masson, D. G. (2003). Canary Islands landslides and tsunami generation, can we use turbidite deposits to interpret landslide processes. In J. Locat, & J. Mienert (Eds.), *Submarine Mass Movements and their Consequences, Advances in Natural and Technological Hazards Research* (Vol. 19, pp. 325–332).

Youngs, R. R., & Coppersmith, K. J. (1985). Implications of fault slip rates and earthquake recurrence models to probabilistic seismic hazard estimates. *Bulletin of the Seismological Society of America, 75*, 939–964.

Zitellini, N., Mendes, L. A., Cordoba, D., Danobeitia, J., Nicolich, R., Pellis, G., et al. (2001). Source of 1755 Lisbon earthquake and tsunami investigated. *Eos Transactions, 82*, 285–291.

Zitellini, N., Rovere, M., Terrinha, P., Chierici, F., Matias, L., Medes-Victor, L., et al. (2004). Neogene through quaternary tectonic reactivation of SW Iberian passive margin. *Pure and Applied Geophysics, 161*, 565–587.